MAX-PLANCK-INSTITUT FÜR PLASMAPHYSIK

GARCHING BEI MÜNCHEN

High β and toroidal effects on the internal kink mode in tokamaks

R. Schmalz

IPP 6/215 September 1982

Die nachstehende Arbeit wurde im Rahmen des Vertrages zwischen dem Max-Planck-Institut für Plasmaphysik und der Europäischen Atomgemeinschaft über die Zusammenarbeit auf dem Gebiete der Plasmaphysik durchgeführt.

IPP 6/215 R. Schmalz High β and toroidal effects on the internal kink mode in tokamaks

September 1982
(in English)

Abstract

The inclusion of high-β and first-order toroidal terms in the reduced set of (resistive) MHD equations affords the possibility of improving the study of tokamak plasma behaviour by three-dimensional numerical simulation. A new code, GALA, based on the reduced equations is developed. It is used to analyse the linear and nonlinear behaviour of the internal kink mode in equilibria which are generated by a simple relaxation procedure. We find that the inclusion of toroidal effects in high-β equilibria provides considerable stabilization.

High β and toroidal effects on the internal kink mode in tokamaks

Contents page

I. Introduction

For the analysis of tokamak and stellarator equilibria, a powerful method has been developed in the last few years. By expanding in the inverse aspect ratio $\varepsilon << 1$ the reduced MHD equations, rid of the fast magnetosonic processes, were derived. Thus numerical analysis is much easier and dynamical studies in three dimensions are more tractable.

For tokamaks, the reduced equations were first derived in the special case of low pressure ($\beta=0(\varepsilon^2)$) in cylindrical geometry (Strauss 1976, Rosenbluth et al. 1976). Strauss (1977) generalized to high β plasmas in cylindrical approximation and Edery et al. (1979) as well as Carreras et al. (1980) included effects of finite aspect ratio in the low β case. The most general reduced equations including both high β and first order toroidal effects were derived by Schmalz (1981a).

In this paper we report on the first application of these generalized equations in a three-dimensional nonlinear code GALA. In section II, the reduced equations are presented. In section III, axisymmetric equilibria are created by a relaxation procedure. Linear and nonlinear stability, especially for the (n=1) - mode is studied in sections IV and V. In section VI we draw some conclusions.

II. The Reduced Equations

Our length scale is the minor radius a which is ε times the major radius R_o. The time scale is the toroidal Alfvén transit time R_o/v_A. Assuming the consistent ordering $B_\phi = O(1)$, $B_\perp = O(\varepsilon)$, $v_\perp = O(\varepsilon)$, $v_\phi = O(\varepsilon^2)$, $\beta = O(\varepsilon)$, we derive to first order in ε

$$\frac{\partial \psi}{\partial t} = - \Phi_{,\phi} + \frac{R^2}{\varepsilon} \underline{B}_\perp \cdot \nabla U + \frac{\eta}{\varepsilon S} \Delta^* \psi + \Phi_o \tag{1}$$

$$\frac{DW}{Dt} = \frac{R^2}{\varepsilon} \left(\underline{B} \cdot \nabla \Delta^* \psi + \frac{\beta}{\varepsilon} \left(2 \left[R, p \right] - \underline{j} \cdot \nabla p \right) \right) \tag{2}$$

$$\frac{Dp}{Dt} = 2 \gamma p \left[U, R \right] \tag{3}$$

$$\Delta^* \Phi = - (1 - \beta p) \Delta^* U + \beta \nabla p \cdot \nabla_\perp U \tag{4}$$

$$\Delta_\perp \chi = \frac{\beta}{\varepsilon} \frac{P}{R^2} \tag{5}$$

$$\Delta_\perp U = \frac{W}{R^2} \quad . \tag{6}$$

The meanings of the symbols are

$$\underline{B} = \nabla \psi \times \nabla \phi + \varepsilon^2 \nabla_\perp \chi_{,\phi} + \frac{1 - \varepsilon R^2 \Delta_\perp \chi}{R} \underline{e}_\phi$$

$$\underline{j} = - \frac{\beta}{\varepsilon} \nabla p \times \nabla \phi + \frac{\varepsilon^2}{R^2} \nabla_\perp \psi_{,\phi} - \Delta^* \psi \nabla \phi$$

$\underline{B}$ = magnetic induction ($_\perp$ means poloidal)
$\underline{j}$ = current density
ψ = poloidal flux / 2π
W = toroidal vorticity
U = velocity stream function
Φ = electrostatic potential
p = pressure
χ = diamagnetic potential
η = resistivity

$$\beta := \frac{\mu_o p_o}{B_o^2} \quad , \quad S := \frac{\mu_o a v_A}{\eta_o} \quad , \quad v_A := \frac{B_o}{\sqrt{\mu_o \rho_o}} \quad , \quad \gamma = 5/3 \; .$$

We use cylindrical coordinates (R,y,ϕ) with $R = 1+\varepsilon x$. All variables are dimensionless and of order one, the ε dependence is explicitly noted. So we have e.g. $\nabla\phi = \frac{\varepsilon}{R}\,\underline{e}_\phi$ and all ε's in the denominators cancel.

The operators are defined by

$$\frac{Df}{Dt} := \frac{\partial f}{\partial t} + R\,[f, U],$$

$$f_{,\phi} := \frac{\partial f}{\partial \phi},$$

$$\Delta_\perp := \frac{\partial^2}{\partial x^2} + \frac{\partial^2}{\partial y^2} + \frac{\varepsilon}{R}\frac{\partial}{\partial x} \quad \text{and}$$

$$\Delta^* := \Delta_\perp - 2\,\frac{\varepsilon}{R}\frac{\partial}{\partial x}.$$

$$[f,U] := \nabla f \times \nabla U \cdot \underline{e}_\phi = \frac{\partial f}{\partial x}\frac{\partial U}{\partial y} - \frac{\partial f}{\partial y}\frac{\partial U}{\partial x}$$

is a useful abbreviation because of certain invariance properties under coordinate transformations. The poloidal velocity has the form

$$\underline{v}_\perp = R^2\,\nabla U \times \nabla\phi .$$

Our philosophy is to keep as far as possible exact terms like R^2 instead of expanding them to the required order. This should help to improve the equations further.

The equations (1) - (6) contain two simplifications. First, it is possible to keep v_ϕ in order ε and solve one further equation for v_ϕ. However, Strauss (1977) has shown that this order vanishes as long as $\underline{B}\cdot\nabla p = 0$. We assume that this condition is fulfilled, if necessary by additional fast nonideal effects like thermal conductivity along the magnetic field. Thus the v_ϕ - equation remains decoupled. Second, we solve the continuity equation for the mass density by simply setting $\rho = \frac{1}{R^2}$. These assumptions leave us with six equations for the six quantities ψ, W, U, p, Φ and χ. Only three of them are time-dependent of mixed type, the others require the solution of elliptic operators.

In the appendix, we write the equations 1 - 6 in general curvilinear coordinates (ρ, θ, ϕ). This is for later use of flux coordinates.

III. Equilibria

As a first step and to gain the input for the dynamical calculations, we generate stationary axisymmetric, toroidal resistive equilibria. In this case, equations (1), (2), (3) and (6) are solved with $\frac{\partial}{\partial \phi} = 0$ and boundary conditions $\psi = 0$, $W = 0$, $U = 0$ and $p = 0$ at the wall. We give a class of initial current profiles of the type

$$j_\phi = j_o \cos\left(\frac{\pi}{2}x\right) \cos\left(\frac{\pi}{2}y\right) e^{-\mu(x^2 + y^2)}$$

and relax by adding an artificial viscosity term $\nu \Delta_\perp W$ in eq. (2) which removes kinetic energy. The pressure is initially set proportional to ψ^2.

In phase I, the resistivity $\eta_o = \frac{1}{\varepsilon S}$ equals zero and is switched on in phase II after the ideal MHD equilibrium has established. Then, a time dependent $\eta = \frac{\psi_o}{j_o} \frac{1}{\psi}$ is inserted and the resistive (quasi-) equilibrium develops.

For these calculations, an Eulerian code was advanced on a Cartesian mesh. The interval was $-1 \leq x \leq 1$ and $-1 \leq y \leq 1$ with up to 256×256 points. Eq. (6) was rearranged to

$$\frac{\partial^2 U}{\partial x^2} + \frac{\partial^2 U}{\partial y^2} = \frac{W}{R^2} - \frac{\varepsilon}{R} \frac{\partial U}{\partial x}$$

and solved by the Buneman algorithm (Buneman 1969) with iteration on the r.h.s. The mean number of iterations $\bar{k}$ for $\varepsilon = .2$ is plotted versus accuracy δ in fig. 1. The time iterations were done by a simple explicit two-step procedure:

$$W^{t+1/2} = W^{t-1/2} + \Delta t\left(R\left[U^{t-1/2}, W^{t-1/2}\right] + R\left[\Delta^* \psi^t, \psi^t\right] + 2\frac{\beta}{\varepsilon} R^2 \left[x, p^t\right] + \nu \Delta_\perp W^{t-1/2}\right), \tag{7}$$

$$U^{t+1/2} = \Delta_\perp^{-1}\left(W^{t+1/2}/R^2\right), \tag{8}$$

$$\psi^{t+1/2} = \psi^t + \frac{\Delta t}{2} R\left[U^{t+1/2}, \psi^t\right], \tag{9}$$

$$\psi^{t+1} = \psi^t + \Delta t\left(R\left[U^{t+1/2}, \psi^{t+1/2}\right] + \eta_o \eta^{t+1/2} \Delta^* \psi^{t+1/2} + \Phi_o\right) \tag{10}$$

$$p^{t+1/2} = p^t + \frac{\Delta t}{2} \left(R \left[\underline{U}^{t+1/2}, p^t\right] + 2\varepsilon\gamma p^t \left[\underline{U}^{t+1/2}, \underline{x}\right]\right) \qquad (11)$$

$$p^{t+1} = p^t + \Delta t \left(R \left[\underline{U}^{t+1/2}, p^{t+1/2}\right] + 2\varepsilon\gamma p^{t+1/2} \left[\underline{U}^{t+1/2}, \underline{x}\right]\right). \qquad (12)$$

Eq. (7) contains a non-centered term which is in all cases small. The inversion of the Laplace - Operator (eq. (8)) is of course the most time consuming part of the computation. In the early phase of the relaxation, the main time step limitation comes from the viscosity according to

$$\Delta t/(\Delta x)^2 \leqq \frac{1}{4\nu} \quad .$$

In phase II, ν was considerably reduced below η_o and the time step was limited by the resistivity especially in the outer regions of the integration domain where η was large to simulate vacuum conditions. Here some improvement was achieved by using the Du Fort - Frankel technique in eq. (10). Sometimes weak dissipation is needed to couple the different meshes together.

To illustrate the effects of resistivity on equilibrium, we compare figs. 2, 3 and 4. Here we have plotted contour lines of ψ, Rj_ϕ and p as well as a vector plot of $\underline{v}_\perp$ and a 3-D plot of j_ϕ. In fig. 2 a high β ideal MHD equilibrium has established with the typical current sheet and reversal to the right. The initial current profile was rather peaked (μ=5). In fig. 3 the end of phase II is shown with a high resistivity $\eta_o = 10^{-3}$. As the computation time T = 200 is comparable with the resistive timescale in this example, the j_ϕ - profile has the tendency to adjust to the η^{-1}- profile. By contrast, in fig. 4 the original current profile is conserved because of the low resistivity $\eta_o = 10^{-5}$. Only the edges have smoothed out. In this case, the two timescales are safely separated. This seems necessary in order to get clear answers by the dynamical calculations. The q-profiles in the case $\mu = 5$ are shown in fig. 5 for both low and high η in the case $\varepsilon = \beta = 0$. In fig. 6 the shift due to ε and β effects is demonstrated. The safety factor on the magnetic axis q_o with which we end up in a particular run depends not only on j_o but on the resistivity.

Fig. 7 shows this dependence which is clearly ~ $1/j_o$ for $\eta_o = 0$ but somewhat complicated for higher η_o. Some more examples of such self-consistent resistive equilibria are given in Schmalz (1981 b).

IV. Linear Stability

In order to investigate the stability of the computed equilibria, a three-dimensional code GALA (= Garching's Large Aspect code) was developed. With its help we are able to study the linear and nonlinear behaviour of low and high β plasmas including toroidal curvature effects in tokamaks. In this section we concentrate on linear stability.

a) Qualitative Description

In principle, the computed equilibria of section III are perturbed to a small extent and the three-dimensional evolution of all quantities is traced in time. In linear stability analysis, the equilibrium fields are kept fixed and the equations are linearized. After an initial adaptation phase, the perturbations develop self-similarly ~ $e^{\Gamma t}$ and for $\Gamma > 0$ the linear theory breaks down at some time or other. The momentary growth rate $\Gamma = \frac{d\ln f}{dt}$ is derived at each time step for the perturbation $f = \psi^{(1)}$ and, independently, for the kinetic energy, which grows at the rate 2Γ. Figure 8 shows a typical example of an unstable mode. The response of a stable equilibrium to a perturbation is only manifested as oscillation like those in fig. 9.

The linear code was written in two versions. In one of them the fields are Fourier analysed in the toroidal direction and only the n = 1 contribution is retained. This is especially effective for the analysis of n = 1 modes. The other version uses finite differences in ϕ, too. This was mainly used for testing the accuracy. Typically, the three-dimensional grid was 32 × 32 × 15 or 64 × 64 × 13 mesh points. The limitations were imposed by the storage capacity available in Garching's CRAY-1 and the computer time required. (With the fine mesh, one time step consumed roughly one second of CPU-time.)

With this type of meshes one would expect the m = 1 mode to be best described. So we concentrate our attention on this so-called "internal kink" instability. As a reference mode we consider fig. 10 where the perturbations $\psi^{(1)}$, $Rj^{(1)}$, $p^{(1)}$ and $\underline{v}_\perp^{(1)}$ are plotted in the plane $\phi = 0$. This is the pure mode (m = 1, n = 1) which varies as $e^{i(m\theta - n\phi)} \cdot e^{\Gamma t}$ (θ = poloidal angle).

As an additional diagnostic, we use a subroutine which follows a field line and denotes the points where it pierces a given poloidal plane. This program was made available to us by W. Lotz.

Some examples are given in figs. 11 to 13. In fig. 13, the original island structure is dissolved into a large "ergodic" region. This becomes meaningful in the non-linear calculations.

From fig. 14 we see how the mode structure changes qualitatively if we include toroidal effects: the perturbations are shifted outwards, have a modified structure and new features appearing to the left. This becomes more drastic if we go on to high β as shown in fig. 15a for $\phi = 0$ and in fig. 15b for $\phi = 90^o$. Here the mode hardly resembles the simple m = 1 picture. The perturbation fills more and more of the plasma volume and higher poloidal harmonics are generated. This mode coupling effect becomes even more obvious in the case $q_o > 1$ which is plotted in figs. 16 and 17. Here the (m = 2, n = 1) mode dominates, being plotted in its pure form in fig. 18. This type of instability is called the ballooning mode because it is driven by the plasma pressure in regions of unfavourable field line curvature.

b) Quantitative Results

As a first test of the code we reproduced the well-known stability behaviour of an analytical circular-cylinder equilibrium

$$j = j_o \left(1 - \frac{r^2}{2}\right)^2 , \quad (r^2 := x^2 + y^2)$$

$$\psi = j_o \left(11/36 - r^2(r^4 - 9r^2 + 36)/144\right)$$

$$\eta = \frac{1}{j} .$$

Here the flux surfaces intersect the boundaries $x = \pm 1$ and $y = \pm 1$. For N = 16, 32 and 64 we find (fig. 19) that the growth rate depends rather sensitively and roughly linearly on $\Delta x = 2/N$. This is because there are thin layers which cannot be resolved in coarse meshes. The theoretical growth rate of the internal kink mode is given by $\Gamma = S^{-1/3}$ (Coppi et al. 1976). The converged values of fig. 19 verify this dependence. The ideal MHD mode is marginally stable.

To shed some light on what may happen in such calculations, we report on a phenomenon which occurred when we changed the boundary conditions to ψ = const. at the boundary, with unchanged current distribution. The converged growth rates did not essentially change. However, the numerical errors grew substantially. Most interesting, even the qualitative behaviour changed at $N \simeq 24$. So it seems absolutely necessary to use fine grids and converged growth rates.

On the other hand, in high-β calculations the dependence on Δx was weak. Typically, the growth rates only changed about five per cent when passing from N = 32 to N = 64.

Next we analyse the influence of a viscosity term on the growth rate. From fig. 20 we learn that there is a considerable slowing down of the dynamics for $\nu \gtrsim 10^{-4}$. So we have to keep ν as small as possible. In many cases we were able to do without any dissipation.

For the computed equilibria with $\mu = 5$ we examined the dependence on q_o. The drastic variation apparent from fig. 21 shows that q_o has to be adjusted very carefully. This is not always easy, as becomes evident from fig. 7. Other effects may thus be masked by a rather small variation in q_o and accompanying large variation of Γ.

The main results concerning the linear behaviour of the resistive internal kink mode are summarized in figs. 22 to 24. Here we have plotted Γ versus the peak poloidal beta $\varepsilon\beta_p = 2\,\beta/\varepsilon$. The volume averaged value is

typically 0.2 times the peak value. The parameters are $\eta_o = 10^{-3}$, $\mu = 5$, $q_o = 0.7$ in figs.22 and $\eta_o = 10^{-4}$, $\mu = 2$, $q_o = 0.7$ in fig. 23 . We see that high-β effects alone are destabilizing (curves $\varepsilon = 0$, cf. Holmes et al. 1982), while toroidal effects in themselves tend to stabilize (see fig. 25, $\varepsilon\beta p$ fixed). This is in contrast to the low-β case treated by Carreras et al. (1981, see also Edery et al. 1981). Figure 24 ($q_o = 1.6$, $\mu = 5$, $\eta_o = 10^{-3}$) corresponds to the kink ballooning mode behaviour found by Ogino et al. (1981). Now the combination of both high β and ε generates a considerable stabilization which leads to a completely stable region for moderate $\varepsilon\beta_p$. The curves for $\varepsilon \neq 0$ descend more and more with growing ε and S. In general, for small $\varepsilon\beta_p$ the mode is mainly resistive (giving rise to so-called sawtooth oscillations or internal disruptions) and becomes the resistive internal kink mode for higher $\varepsilon\beta_p$. A further increase of $\varepsilon\beta_p$ should lead to a second stability region where the internal kink mode is stabilized and the tearing mode character reappears as reported by Tokuda et al. (1982). The onset of this stabilization is seen from fig. 22b, where the growth rate begins to decrease for $\varepsilon\beta_p \gtrsim 3$. However, $\varepsilon\beta_p$ - values higher than 4 are hard to obtain.

In the case treated in fig. 23 (ε=.1) the stable region extends from $\varepsilon\beta_p \approx 0.5$ to $\varepsilon\beta_p \approx 1.5$. This stabilization is primarily due to the new interchange terms such as $j \cdot \nabla p$ appearing in the generalized reduced equations.

In this context we wish to comment on the case $\varepsilon \to 0$: In analytical work one often treats a long, straight cylinder with the requirement $ka << 1$, where k is the wave number of the perturbation (see e.g. Rosenbluth et al. 1973). This so-called "large aspect ratio approximation" is in principle different from our "cylindrical" case $\varepsilon \to o$ because for $\varepsilon \neq o$ we always have a curved geometry. This should be kept in mind when comparing results.

V. Nonlinear Calculations

The main advantage of the approach we choose lies in the fact that the code is able to follow the three-dimensional nonlinear evolution of an equilibrium. This is absolutely necessary when the modes are of finite amplitude.

As a reference example, we treat the m = 1 tearing mode in a circular-cylinder equilibrium (see also Waddell et al. 1976). In figs. 26a-e a time series of the mode structure is plotted from T = 60 to T = 180. Here instead of $p^{(1)}$ we plot the helical flux function $\psi^* := \psi + \frac{1}{2}r^2$.
Figure 27 shows the temporal behaviour of the (n=1) perturbation amplitude $\psi^{(1)}(t) := \psi(t) - \psi(t=0)$ and the kinetic energy, their momentary growth rates $\Gamma(\psi)$ and $\Gamma(E)$ and the total energy balance testing the accuracy of the code. We now give a brief description of the mode evolution: By T ≈ 120 the perturbation breaks through the plasma, generating a three-island structure. The safety factor q is raised to a value slightly above one, having a flat profile in the inner part. The current profile $j_\phi(x)$ (plotted in fig. 28 at T = 105) changes from peaked to flat, peaks somewhat again and so on. Up to T ≈ 200 the mode thus oscillates several times. The final state looks like fig. 26e and exhibits no circular symmetry. From fig. 27 it is seen that the evolution of the mode up to T ≈ 50 is very similar to that in the linear case. The growth rate $\Gamma(\psi^{(1)})$ then begins to drop below $\Gamma(E_{kin})$ and nonlinear effects become important. At T ≈ 90 $\psi^{(1)}$ reaches its maximum amplitude and then declines somewhat by T ≈ 120. At this time the kinetic energy is largest. The mode now grows again etc.

In general, it was found that the circular-cylinder equilibria were easier to handle than the noncircular ones. The nonlinear evolution of the latter led in low β cases to full reconnection of the magnetic field lines, leaving a large ergodic region inside the q = 1 surface like in fig. 29.

However, when the linear growth rates were sufficiently reduced by coupling of high β and toroidal effects, nonlinear saturation was observed. As an example, we consider the case $\varepsilon = .15$ and $\varepsilon\beta p = .5$. In fig. 30 the saturated island structure is revealed. Besides the $m = 1$ mode, there is a contribution from $m = 2$ localized near the $q = 1$ surface. The saturated island width is roughly one-tenth of the minor radius. A small (m=3, n=2) mode is also visible. However, the central region is hardly affected by the perturbation. This is clearly a high-β effect similar to that reported by Holmes et al. (1982) in the limit $\varepsilon \to 0$. Now we are able to influence the process by varying the aspect ratio. Qualitatively, we find that the behaviour of the $n = 1$ instability is almost completely determined by the plasma β. The main toroidal effects are

- lengthening of the time scales as suggested by the linear calculations,
- generation of higher - order modes via toroidal mode coupling.

The appearance of higher-order modes driven by low-m perturbations is a common phenomenon in nonlinear and toroidal calculations. A further example is given in figs. 31 a,b , where the parameters are $\varepsilon = .2$ and $\varepsilon\beta_p = 2$. Besides the initial (m=1, n=1) mode there are clearly contributions from (m=3, n=2) and (m=2, n=1) at T = 90. These grow fast and overlap, and at T = 120 the outer region has already become ergodic. This behaviour is frequently observed and indicates the importance of the higher order modes, especially in our geometry. However, the adequate numerical treatment of these modes must await the introduction of flux coordinates.

In general, the reasons for studying these effects are evident:

The nonlinear behaviour of the (m=1, n=1) mode is generally believed to explain the "internal disruption" in a tokamak. Ergodic regions lead to enhanced energy transport. The interaction of magnetic islands such as (m=2, n=1) and (m=3, n=2) is suspected of causing the "major disruptions" in tokamaks, which have to be avoided in large devices.

VI. Conclusions

The new code, GALA, based on the generalized reduced equations works satisfactorily:

- The relaxation procedure used to generate high-pressure toroidal (quasi-) equilibria is quite natural and flexible.

- All known effects such as nonlinear saturation, mode coupling, high-β behaviour, etc. are reproduced in three-dimensional dynamical calculations.

- The combination of high-β and toroidal effects provides considerable stabilization.

- Nonlinear saturation saves a high-β plasma core from reconnection.

Nevertheless, the convergence behaviour of such codes advocates caution and, quite generally, the numbers derived with rather coarse meshes should not be taken too seriously.

Acknowledgement:

The author wishes to thank D. Biskamp for many valuable discussions.

VII. Appendix

The reduced equations in general non-orthogonal curvilinear coordinates (ρ,θ) (the toroidal angle ϕ is retained):

Jacobian $\quad \tilde{J} = \sqrt{g} = \nabla\rho \times \nabla\theta \cdot \nabla\phi = \frac{\varepsilon}{R}\,[\rho,\theta]$;

$J := \tilde{J}/\varepsilon$;

Covariant metric coefficients $\quad g^{\rho\rho} = |\underline{\nabla}\rho|^2$;

$g^{\theta\theta} = |\nabla\theta|^2$;

$g^{\rho\theta} = \nabla\rho\cdot\nabla\theta$;

Invariant quantity $\quad J\{f,g\} := J(f_{,\rho}g_{,\theta} - f_{,\theta}g_{,\rho})$

$= \frac{1}{R}\,[\underline{f},\underline{g}]$

Scalar product $\quad (f,g) := \underline{\nabla}f \cdot \underline{\nabla}g = g^{\rho\rho} f_{,\rho} g_{,\rho} + g^{\theta\theta} f_{,\theta} g_{,\theta}$

$+ g^{\rho\theta}(f_{,\rho}g_{,\theta} + f_{,\theta}g_{,\rho})$

In axisymmetry, we have e.g.

$$\frac{1}{\varepsilon}\,\underline{B}_\perp \cdot \nabla f = \frac{1}{R}\,[\underline{f},\underline{\psi}] = J\{f,\psi\}$$

If ρ is a flux coordinate $\rho(\psi)$, $\psi_{,\theta}$ vanishes and

$$\frac{1}{\varepsilon}\,\underline{B}_\perp \cdot \underline{\nabla} f = -J\,\psi_{,\rho}\,f_{,\theta}$$

In general, our equations then sound

$$\frac{\partial\psi}{\partial t} = -\phi_{,\phi} + JR^2\{U,\psi\} + \varepsilon R^2\,(U,\chi_{,\phi}) \tag{1}$$

$$\frac{\partial W}{\partial t} = JR^2\{U,W\} + JR^2\{\Delta^*\psi,\psi\} + (1-\beta p)\,\Delta^*\psi_{,\phi} +$$

$$+ 2\,\frac{\beta}{\varepsilon}\,JR^3\{x,p\} + \beta p_{,\phi}\Delta^*\psi - \beta(p,\psi_{,\phi}) + \varepsilon R^2(\Delta^*\psi,\chi_{,\phi}) \tag{2}$$

$$\frac{\partial p}{\partial t} = JR^2\{U,p\} + 2\varepsilon\gamma pJR\{U,x\} \tag{3'}$$

$$\Delta^* \phi = -(1-\beta p)\,\Delta^* U + \beta(p,U) \tag{4'}$$

$$\Delta_\perp \chi = \frac{\beta}{\varepsilon}\,\frac{P}{R^2} \tag{5'}$$

$$\Delta_\perp U = \frac{W}{R^2} \tag{6'}$$

with

$$\Delta^* f = g^{\rho\rho} f_{,\rho\rho} + g^{\theta\theta} f_{,\theta\theta} + 2g^{\rho\theta} f_{,\rho\theta}$$
$$+ JR^2 f_{,\rho}\left(\left(\frac{g^{\rho\rho}}{JR^2}\right)_{,\rho} + \left(\frac{g^{\rho\theta}}{JR^2}\right)_{,\theta}\right)$$
$$+ JR^2 f_{,\theta}\left(\left(\frac{g^{\rho\theta}}{JR^2}\right)_{,\rho} + \left(\frac{g^{\theta\theta}}{JR^2}\right)_{,\theta}\right)$$

$$\Delta_\perp f = \Delta^* f + \frac{2}{R}\left(U_{,\rho}\left(g^{\rho\rho}R_{,\rho} + g^{\rho\theta}R_{,\theta}\right) + U_{,\theta}\left(g^{\rho\theta}R_{,\rho} + g^{\theta\theta}R_{,\theta}\right)\right).$$

References

Buneman, O., SUIR Report 294, 1969

Carreras, B., Hicks, H.R., Lee, D.K., Phys. Fluids (1981)
Edery, D., Pellat, R., Soule, J.L., Report EUR-CEA-FC-1109,(1981)
Holmes et al., Phys. Fluids 25, 800 (1982)

Ogino et al., J. Phys. Soc. Japan 50, 1698 (1981)

Rosenbluth, M.N., Monticello, D.A., Strauss, H.R., White, R.B.
Physics of Fluids 19, 1987 (1976)
Rosenbluth, M.N., Dagazian, R.Y., Rutherford, P.H.,
Physics of Fluids 16, 1894 (1973)
Schmalz, R.F., Physics Lett. 82 A, 14 (1981 a)
" , Comp. Phys. Comm. 24, 421 (1981 b)
Strauss, H.R., Phys. Fluids 19, 134 (1976)
" " 20, 1354 (1977)
Tokuda, S., et al. Nucl. Fusion Lett, 22, 661 (1982)
Waddell et al., Nucl. Fusion Letters 163, 528 (1976)

Figure Captions:

Fig. 1 Mean number of iterations $\bar{k}$ versus accuracy δ for the solution of the Laplace-like equations using the Buneman algorithm.

Fig. 2-4 Contour plot of poloidal flux ψ, current density Rj_ϕ and pressure p; vector plot of the flow pattern $\underline{v}_\perp$ and 3-D plot of j_ϕ for the parameters given in the lower left corner. β stands for $\frac{\beta}{\varepsilon}$, ψ_M is the maximum of ψ, etc.

Fig. 5 Safety factor q for the peaked (upper curve) and the broadened (lower curve) profile (case $\varepsilon = \beta = 0.$)

Fig. 6 Shift of the q-profile due to toroidal and high-β effects. The parameters are $\beta = 1.$ and $\varepsilon = .2.$

Fig. 7 Dependence of q_o (= q on axis) on j_o and resistivity for $\mu = 5$, $\varepsilon = \beta = 0.$).

Fig. 8+9 Growth rates of the n = 1 component of the flux perturbation $\psi^{(1)}$ and the kinetic energy (dashed line). In fig. 8 an unstable case is considered, whereas in fig. 9 the equilibrium is stable.

Fig. 10 Perturbations $\psi^{(1)}$, $Rj_\phi^{(1)}$, $p^{(1)}$ and $\underline{v}_\perp^{(1)}$ for a pure (m = 1, n = 1) mode. The parameters are listed to the right.

Fig. 11-13 Field line tracing at times T = 50, 100 and 150.

Fig. 14 Corresponding plot of the perturbations. The change in the mode structure is due to toroidal effects.

Fig. 15a,b High-β mode structure at $\phi = 0^\circ$ and $\phi = 90^\circ$.

Fig. 16 Mode structure for $q_o > 1$.

Fig. 17 Field line tracing corresponding to fig. 16. Dominant modes are (m=2, n=1) and (m=3, n=2).

Fig. 18 Pure (m=2, n=1) mode.

Fig. 19a,b Convergence behaviour of the linearized version of the code. The poloidal mesh was given by N = 16,32 and 64 with various η_o - values as indicated. Figure 19b differs from fig. 19a by changing the equilibrium boundary conditions.

Fig. 20 Influence of a viscosity term on Γ.

Fig. 21 Dependence of Γ on q_o for a peaked profile and fixed resistivity.

Fig. 22-23 Linear growth rates versus peak poloidal β. Parameters are $q_o = 0.7$, $\eta_o = 10^{-3}$ in fig. 22 and $\eta_o = 10^{-4}$ in fig. 23. In fig. 22b the value of $<\varepsilon\beta_p>$ is derived from volume averaging.

Fig. 24 Same as fig. 22 for $q_o = 1.6$.

Fig. 25 Dependence of Γ on ε for fixed $\varepsilon\beta_p$.

Fig. 26a-e Nonlinear time evolution of a circular-cylinder equilibrium till T = 200.

Fig. 27 Amplitudes and growth rates corresponding to figs. 26. The third plot demonstrates total energy conservation.

Fig. 28 Toroidal current profile at time T = 105.

Fig. 29a,b Nonlinear evolution of a low-β computed equilibrium leading to full reconnection inside the q=1 surface.

Fig. 30 Saturated state of a high β toroidal equilibrium with $\varepsilon = .15$ and $\varepsilon\beta_p = .5$

Fig. 31a,b Simultaneous development of (m=1, n=1), (m=3, n=2) and (m=2, n=1) modes in a high-β equilibrium.

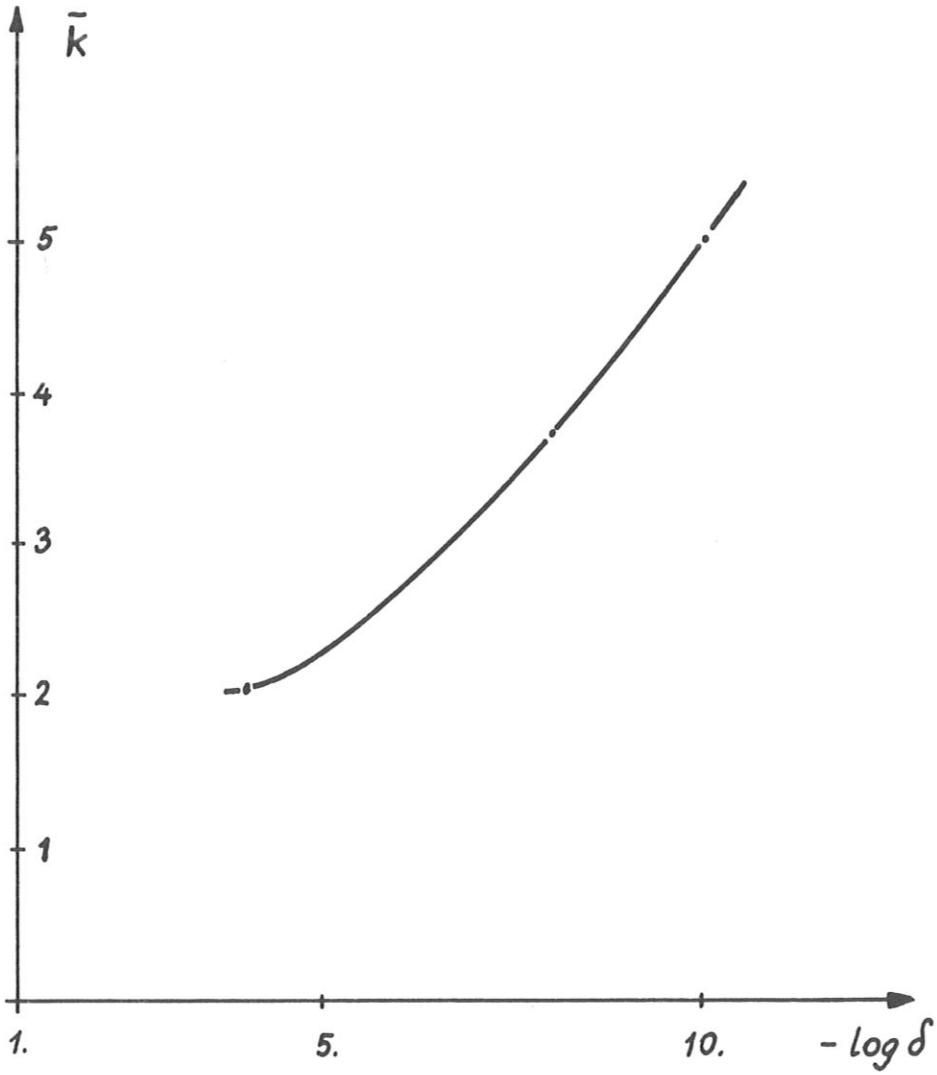

Fig. 1

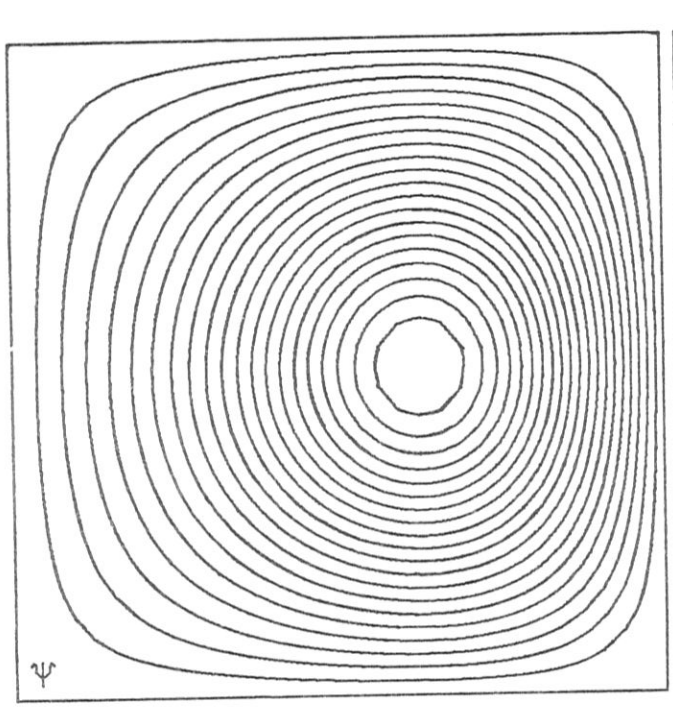

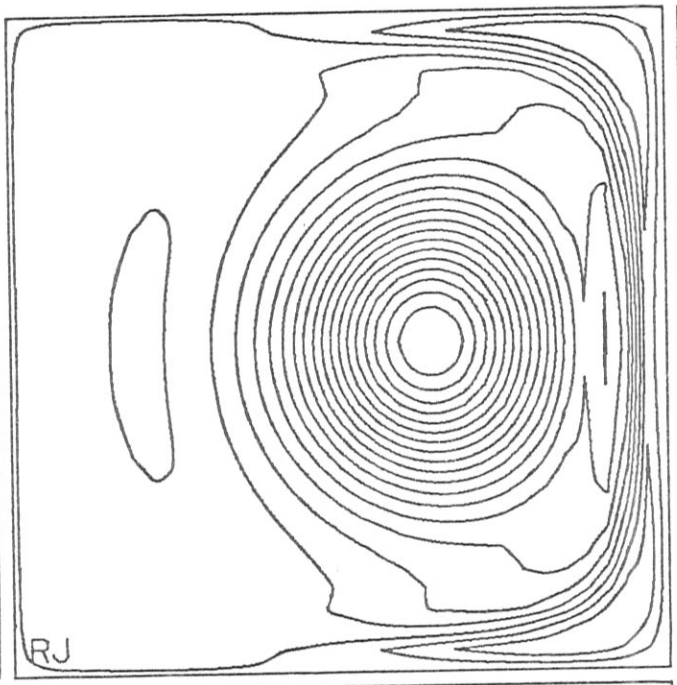

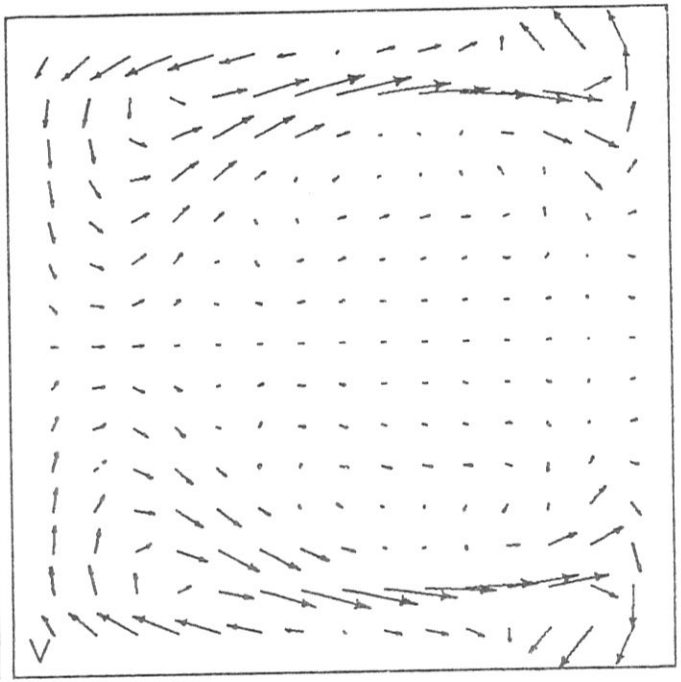

N = 32 Ψ_M = 0.508E 00

ε = 0.200 J_M = 0.480E 01

Δ t = 0.010 U_M = 0.159E-03

β = 1.000 P_M = 0.220E 00

ν = 0.900E-01

η_0 = 0.0 μ = 5

Φ_0 = 0.0

Ψ_0 = 5.000

SUM = 1.000E-05

[p,ψ]=0.123E-02

T = 58.9000

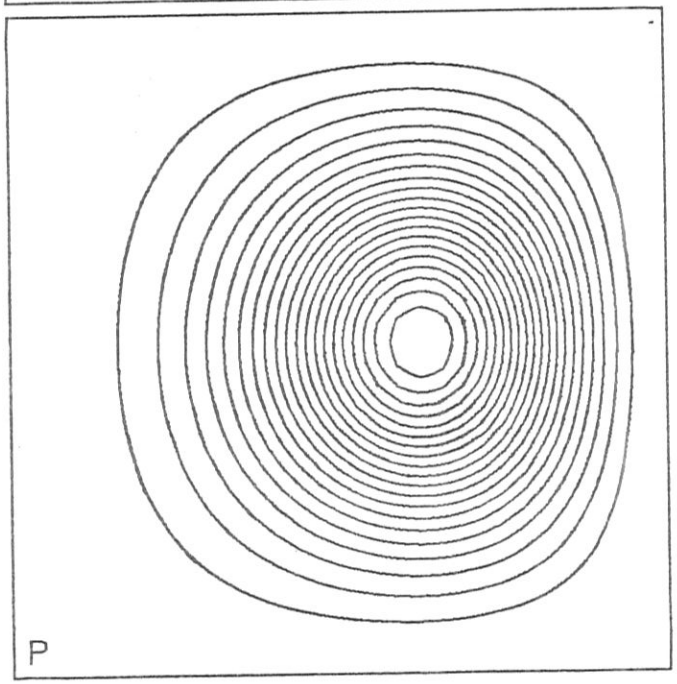

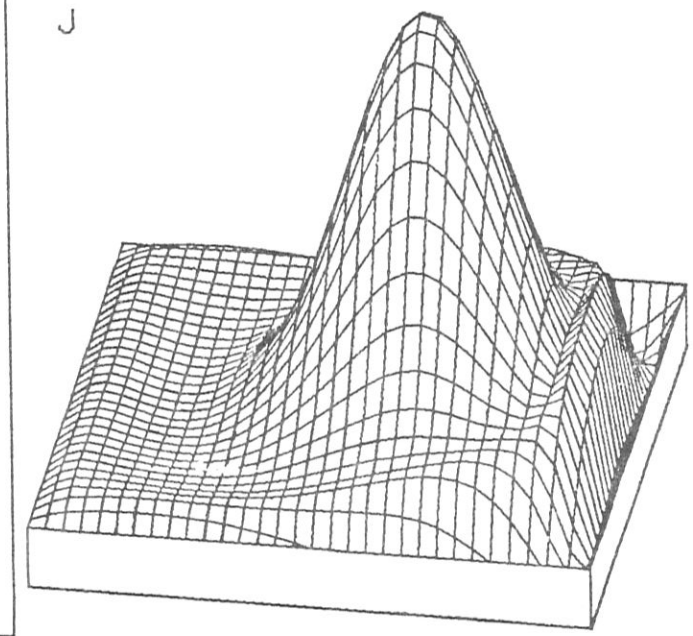

Fig. 2

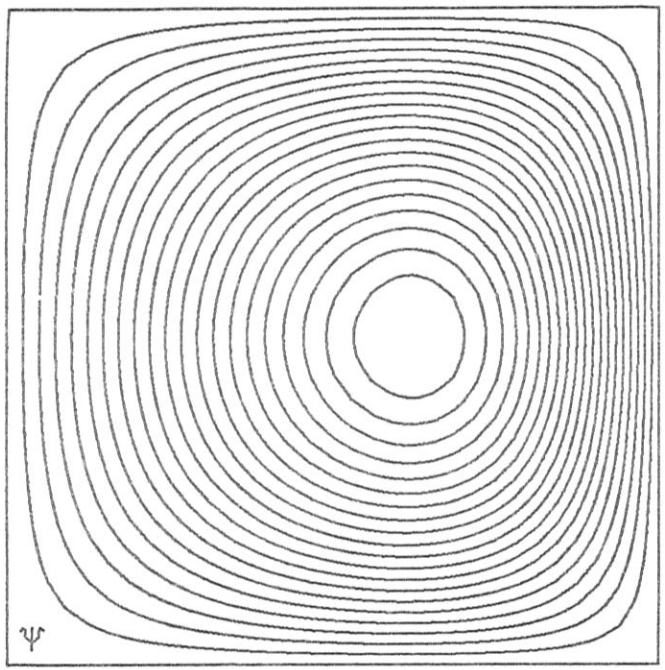

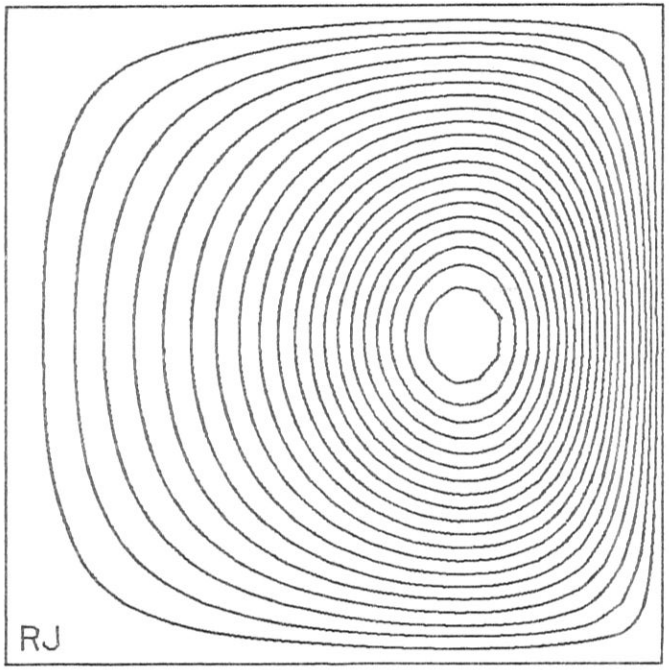

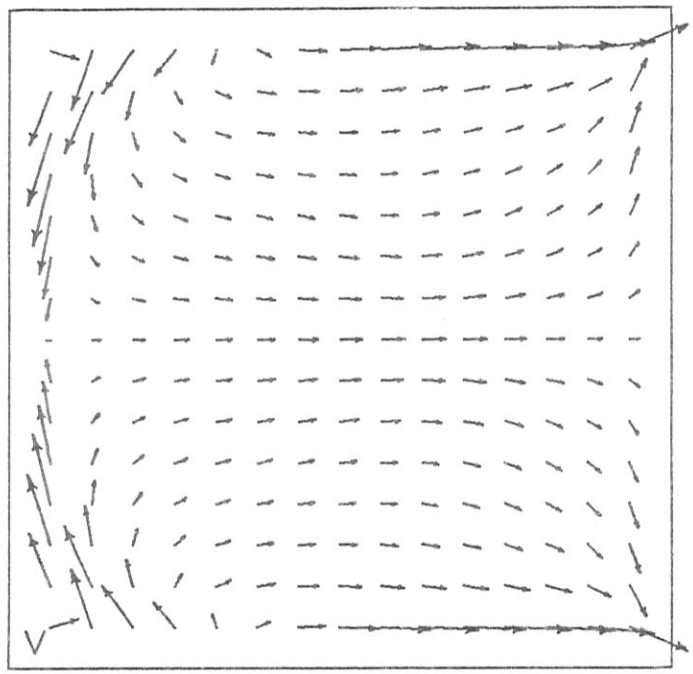

N = 32 Ψ_M = 0.455E 00

ε = 0.200 J_M = 0.295E 01

Δ t = 0.010 U_M = 0.740E-03

β = 1.000 P_M = 0.213E 00

ν = 0.100E-03

η_0 = 0.100E-02 μ = 5

Φ_0 = 0.100E-02

Ψ_0 = 5.000

SUM = 0.840E-05

[p,ψ]=0.691E-02

T = 200.0000

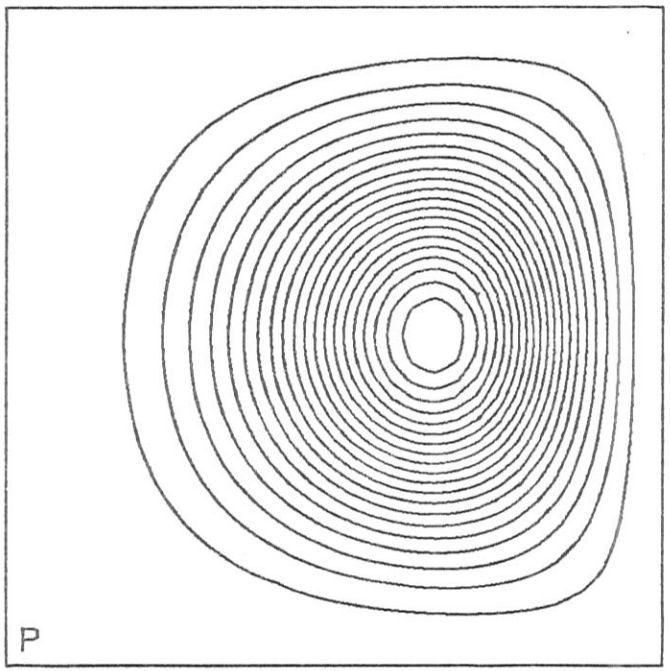

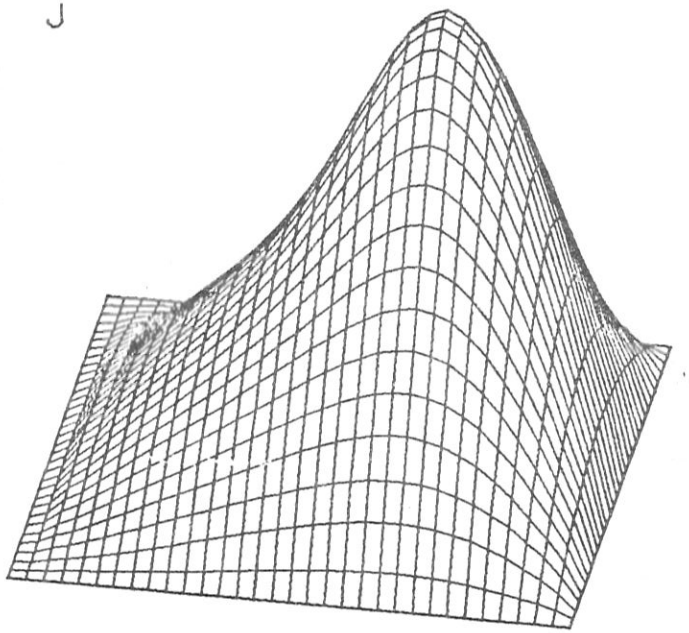

Fig. 3

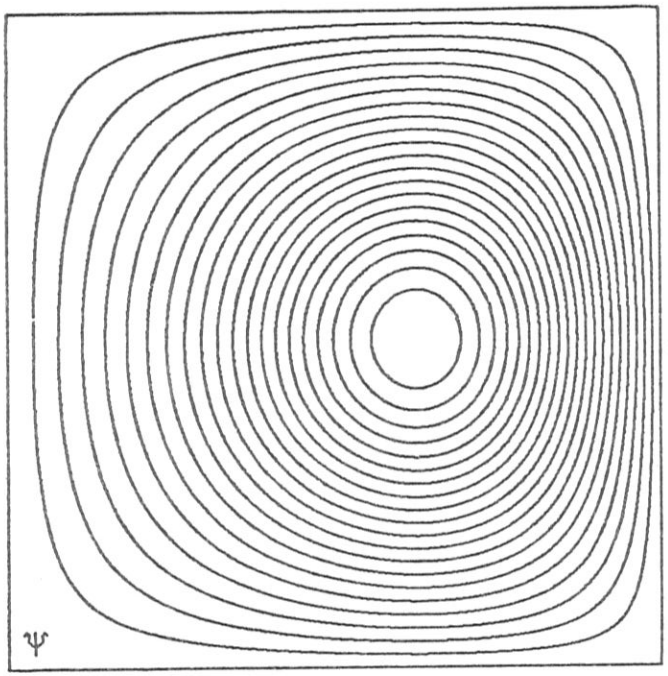

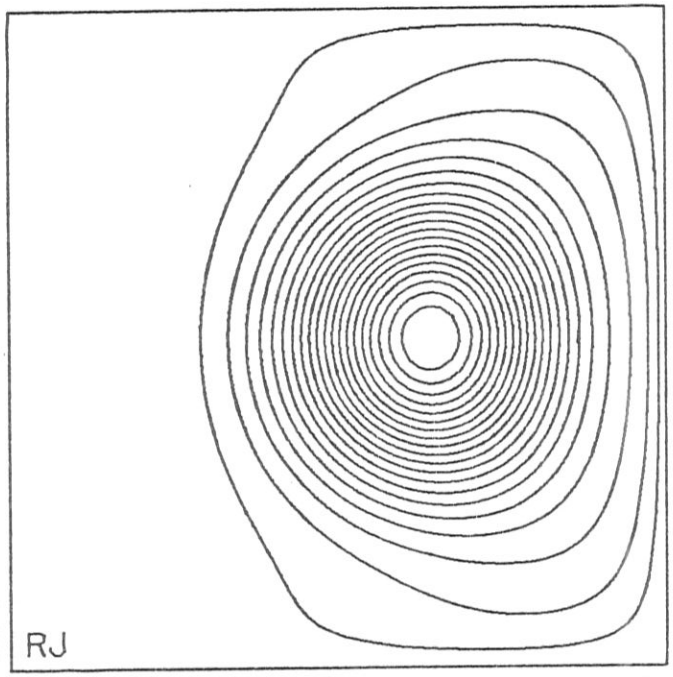

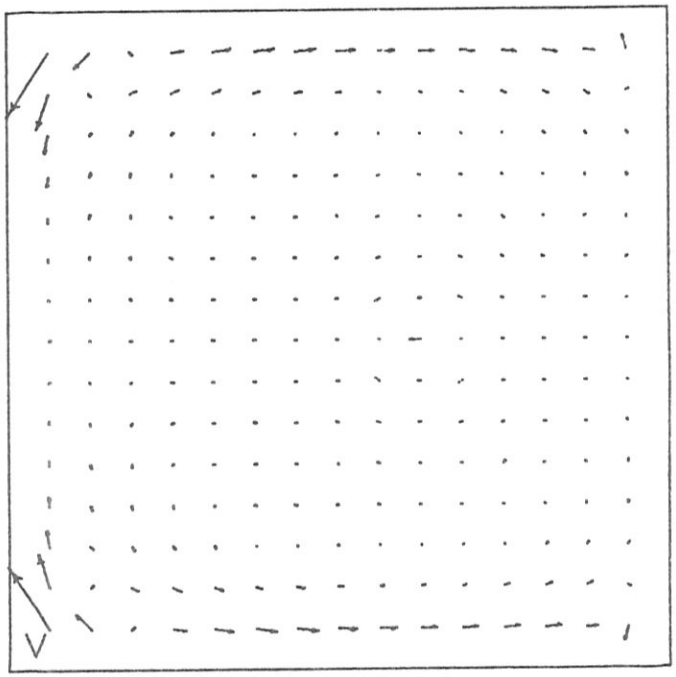

N = 128 Ψ_M = 0.506E 00

ε = 0.200 J_M = 0.478E 01

Δ t = 0.010 U_M = 0.469E-04

β = 1.000 P_M = 0.219E 00

ν = 0.100E-05

η_0 = 0.100E-04 μ = 5

Φ_0 = 0.100E-04

Ψ_0 = 5.000

SUM = 0.317E-05

[p,ψ]=0.116E-02

T = 198.9400

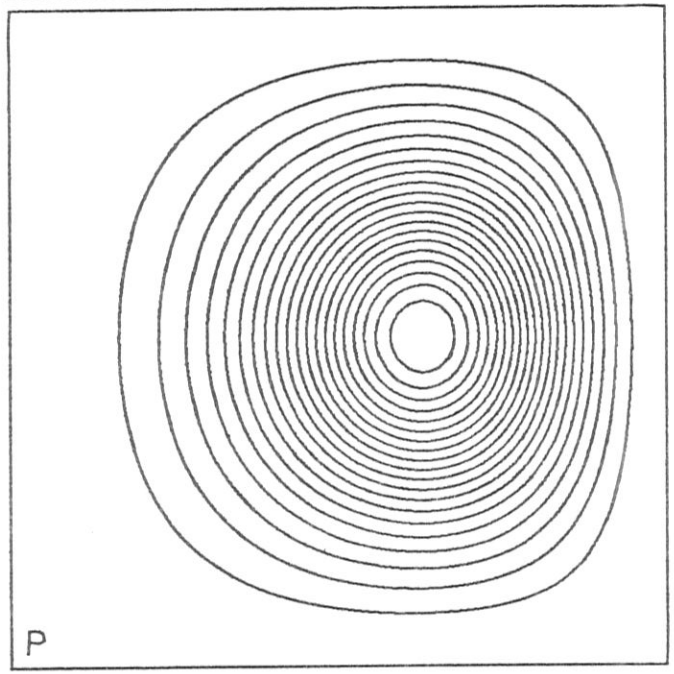

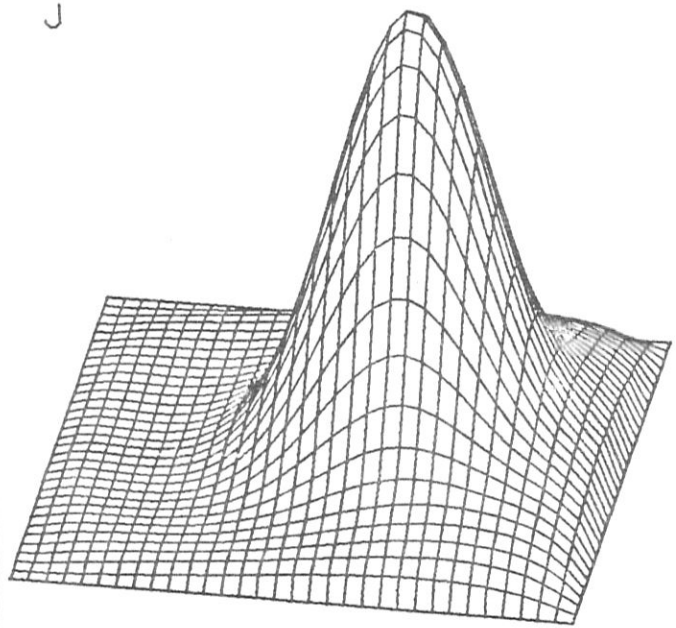

Fig. 4

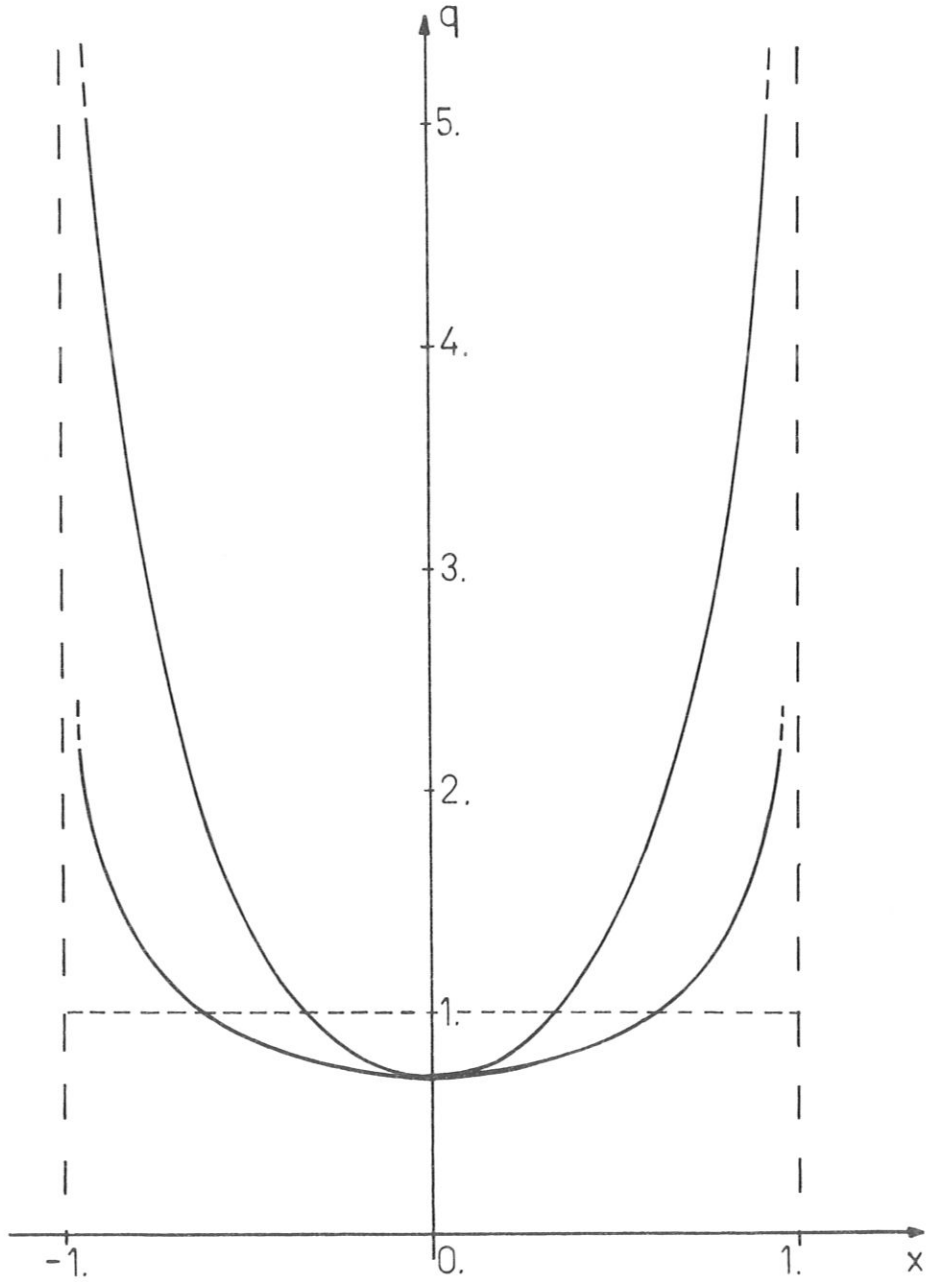

Fig. 5

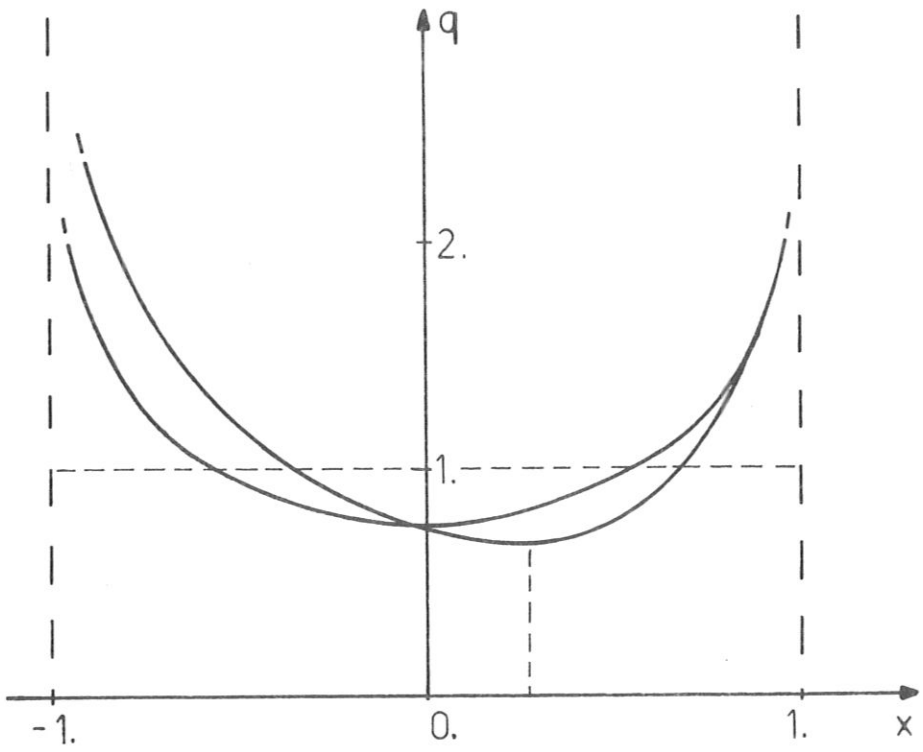

Fig. 6

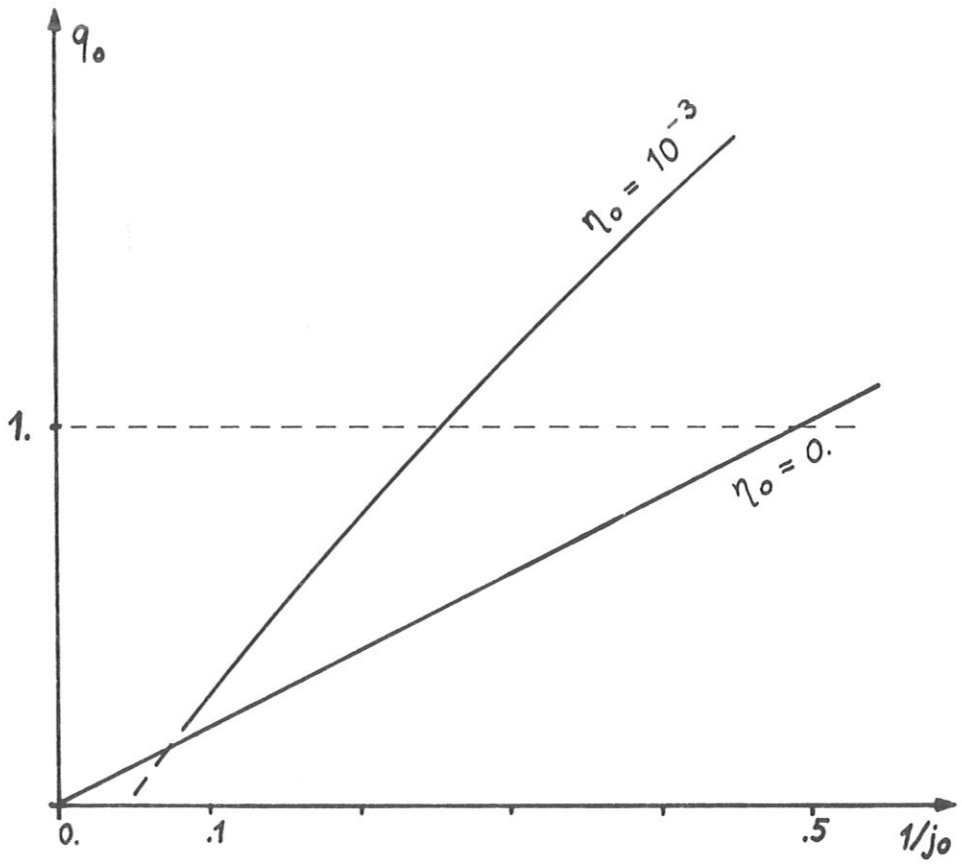

Fig. 7

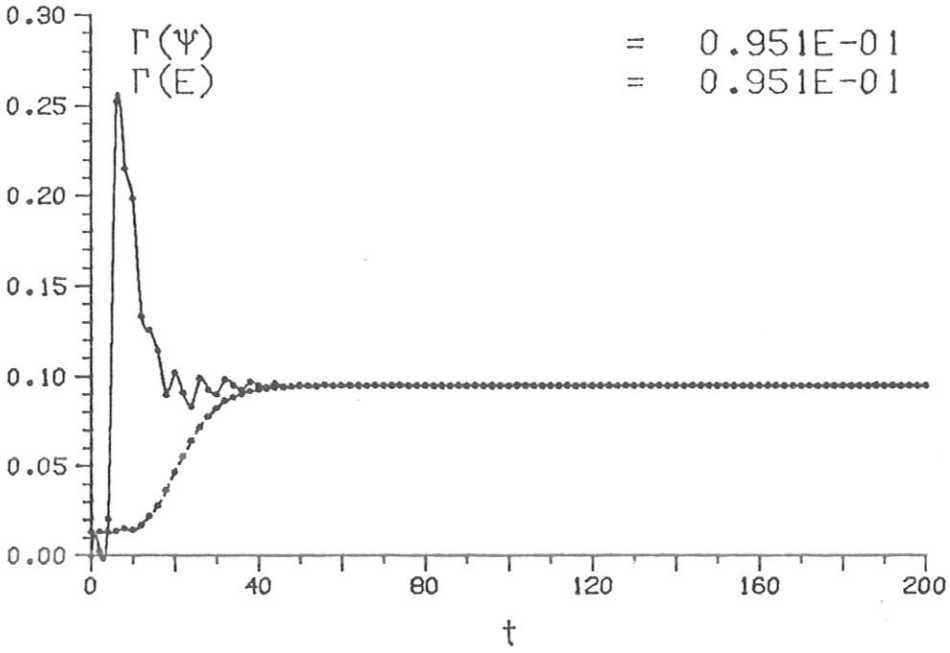
0.30
0.25
0.20
0.15
0.10
0.05
0.00
Γ(Ψ) = 0.951E-01
Γ(E) = 0.951E-01
0
40
80
120
160
200
t

Fig. 8

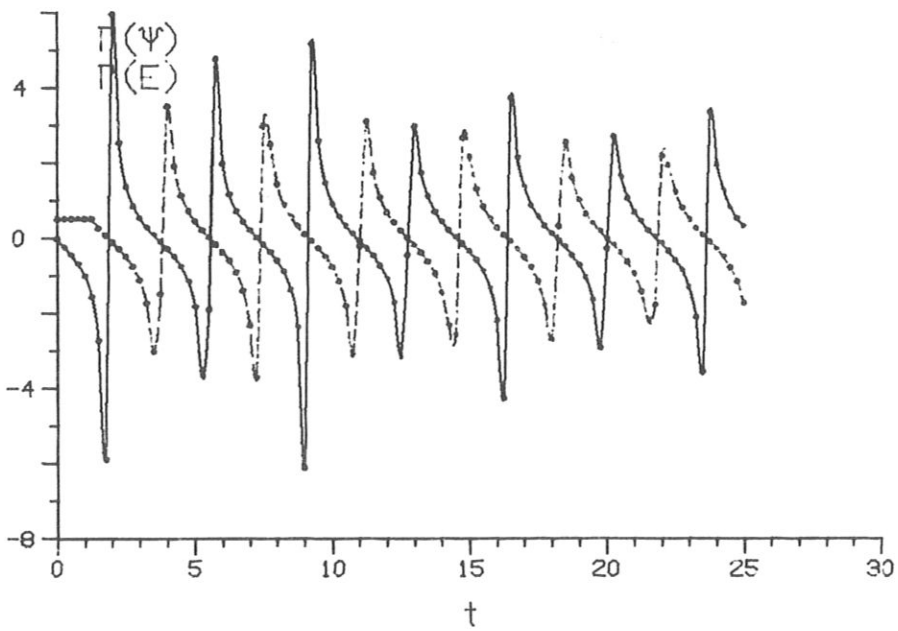
Γ(Ψ)
Γ(E)
4
0
-4
-8
0
5
10
15
20
25
30
t

Fig. 9

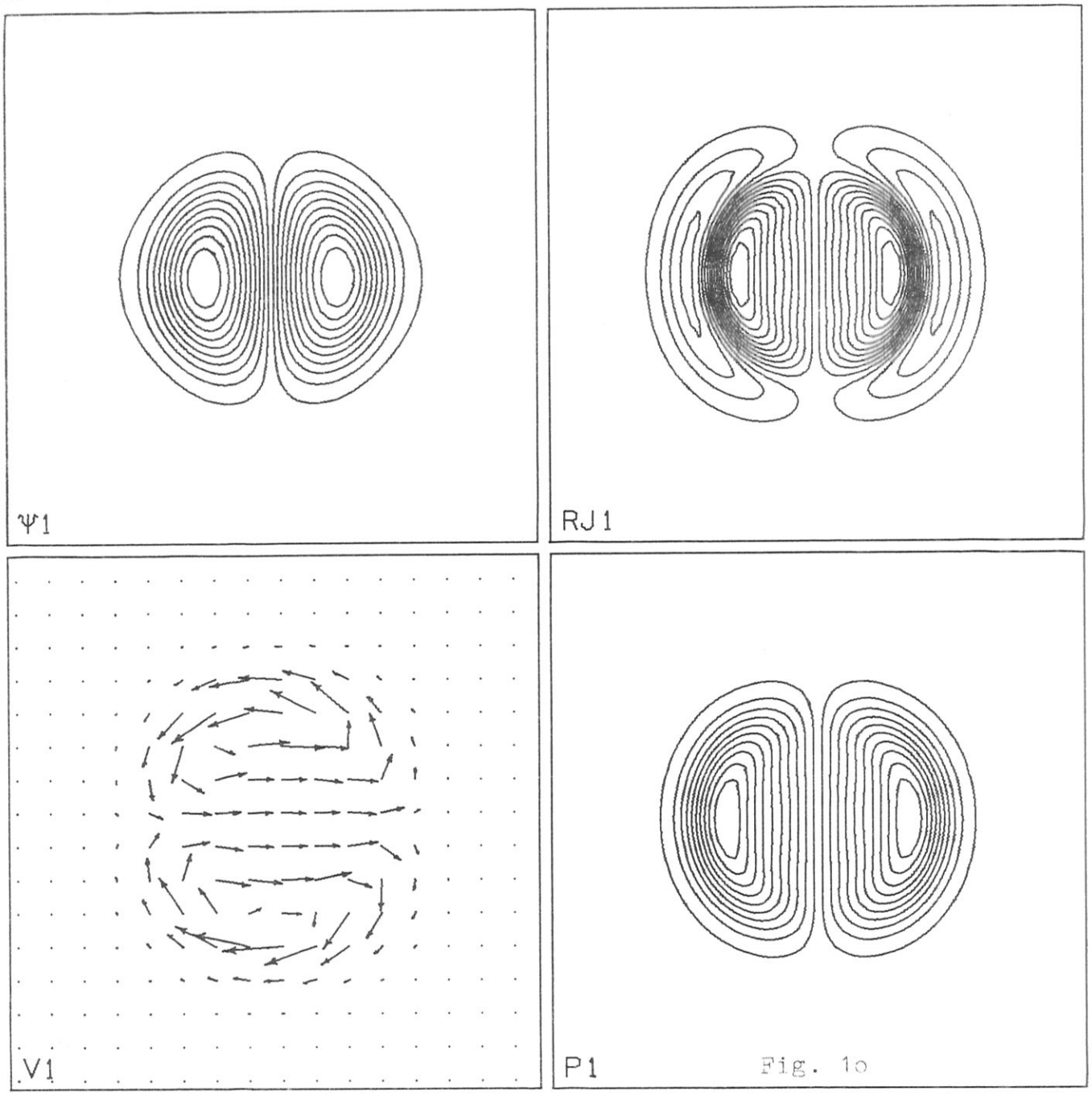

Fig. 1o

N =	64	μ = 2
M =	31	
ε =	0.000	
Δ t =	0.050	
β =	0.000	
ν =	0.0	
η_0 =	0.100E-02	
Φ_0 =	0.100E-02	
J_0 =	2.600	
$\Psi 1_0$ =	0.1000	
φ =	0.000	
T =	100.0000	
$\Psi 1_M$ =	0.185E 00	
$J1_M$ =	0.128E 02	
$U1_M$ =	0.121E 00	
$P1_M$ =	0.162E 01	
m =	1	

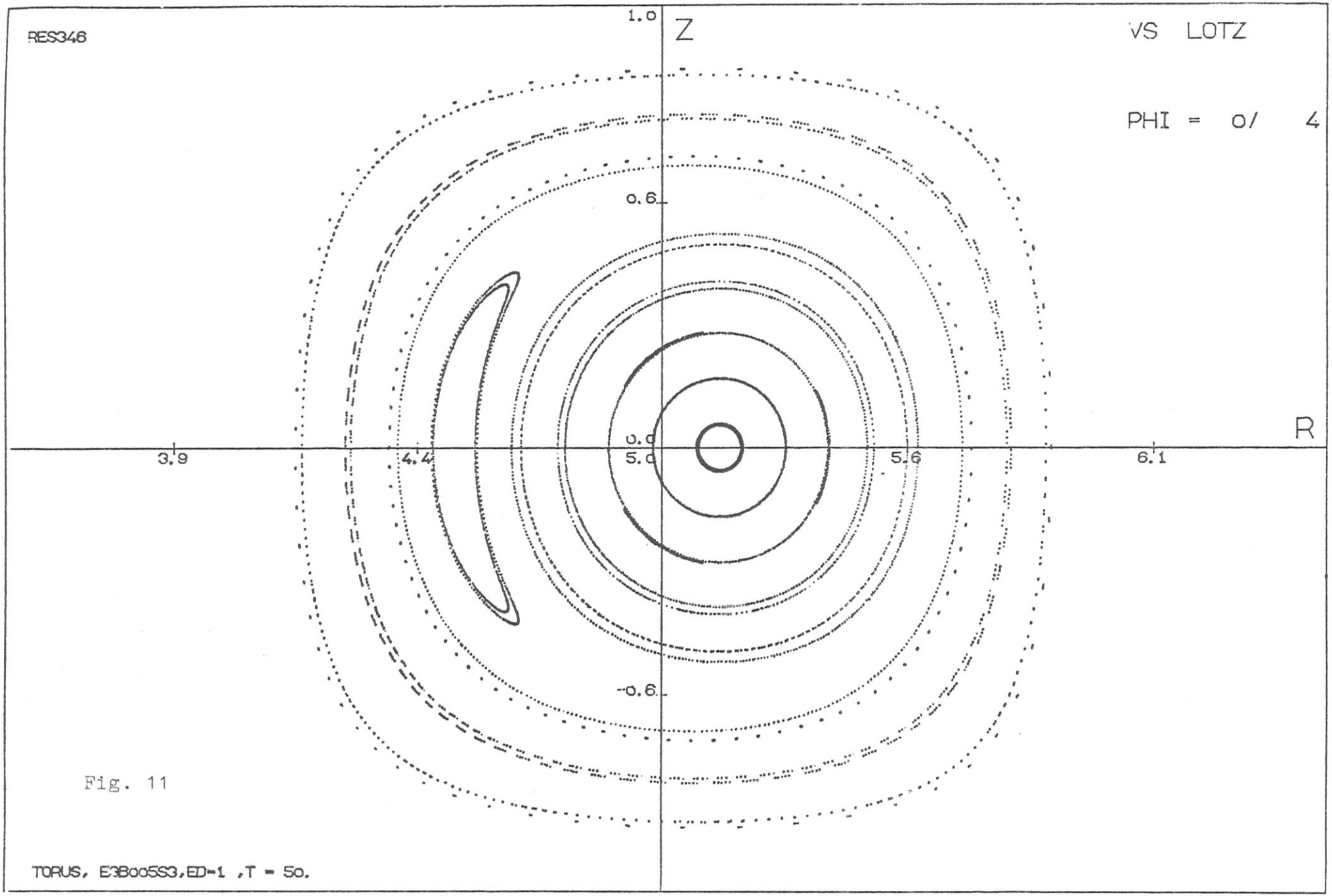
RES346
Z
VS LOTZ
PHI = 0/ 4
1.0
0.6
0.0
-0.6
R
3.9
4.4
5.0
5.6
6.1
TORUS, E3B005S3,ED=1 ,T = 50.

Fig. 11

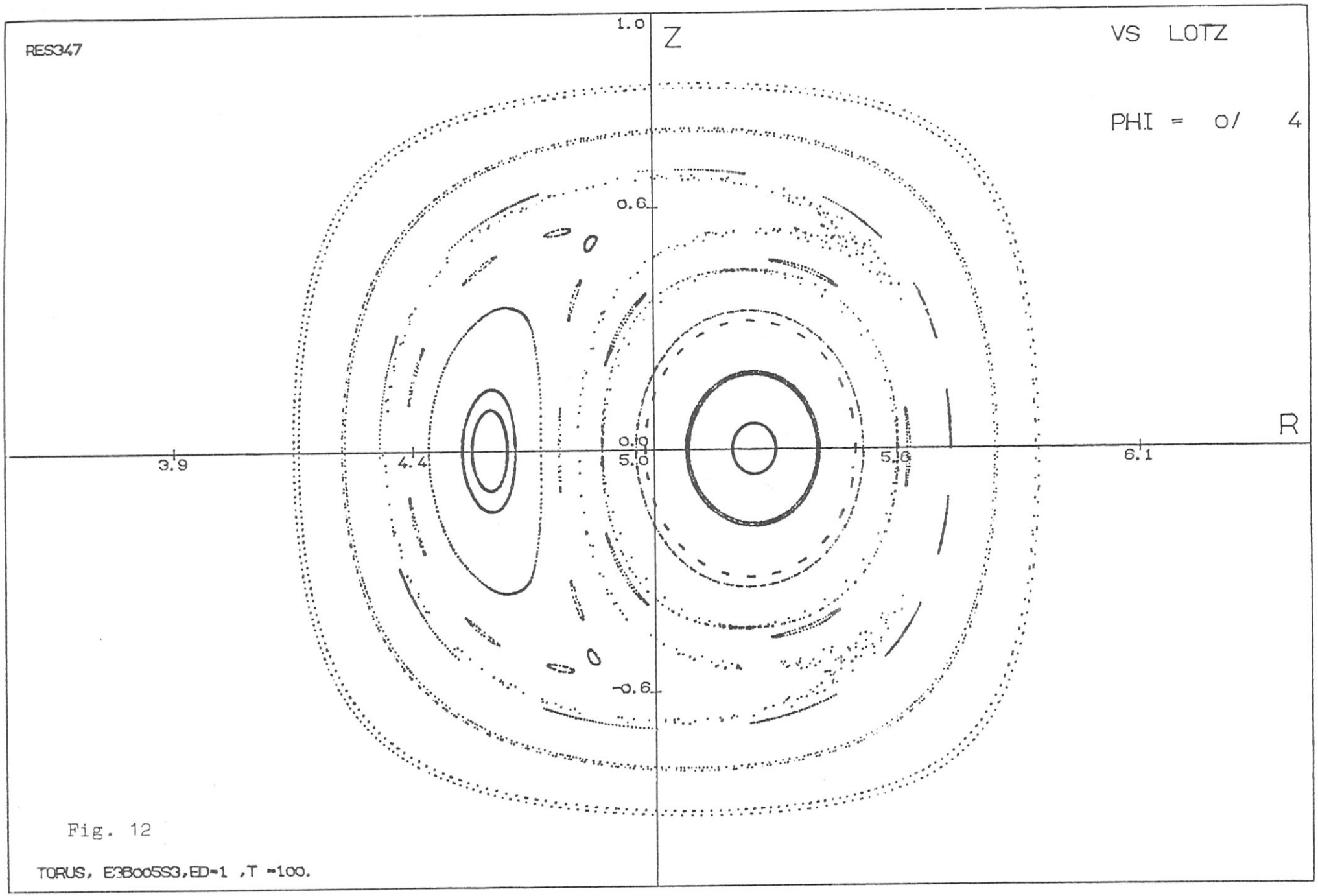

Fig. 12

TORUS, E3B005S3,ED=1 ,T =100.

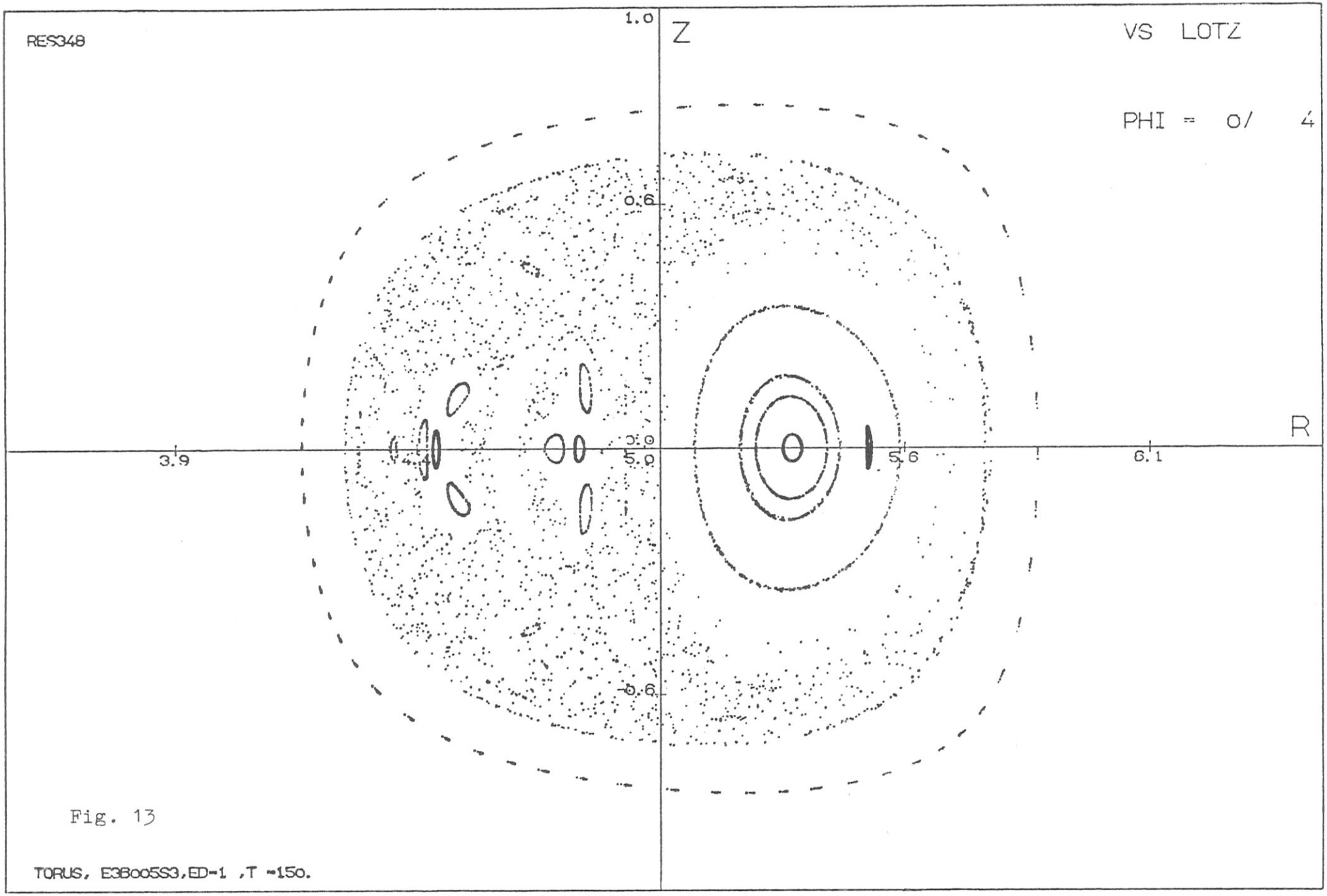

Fig. 13

TORUS, E3B005S3,ED-1 ,T =150.

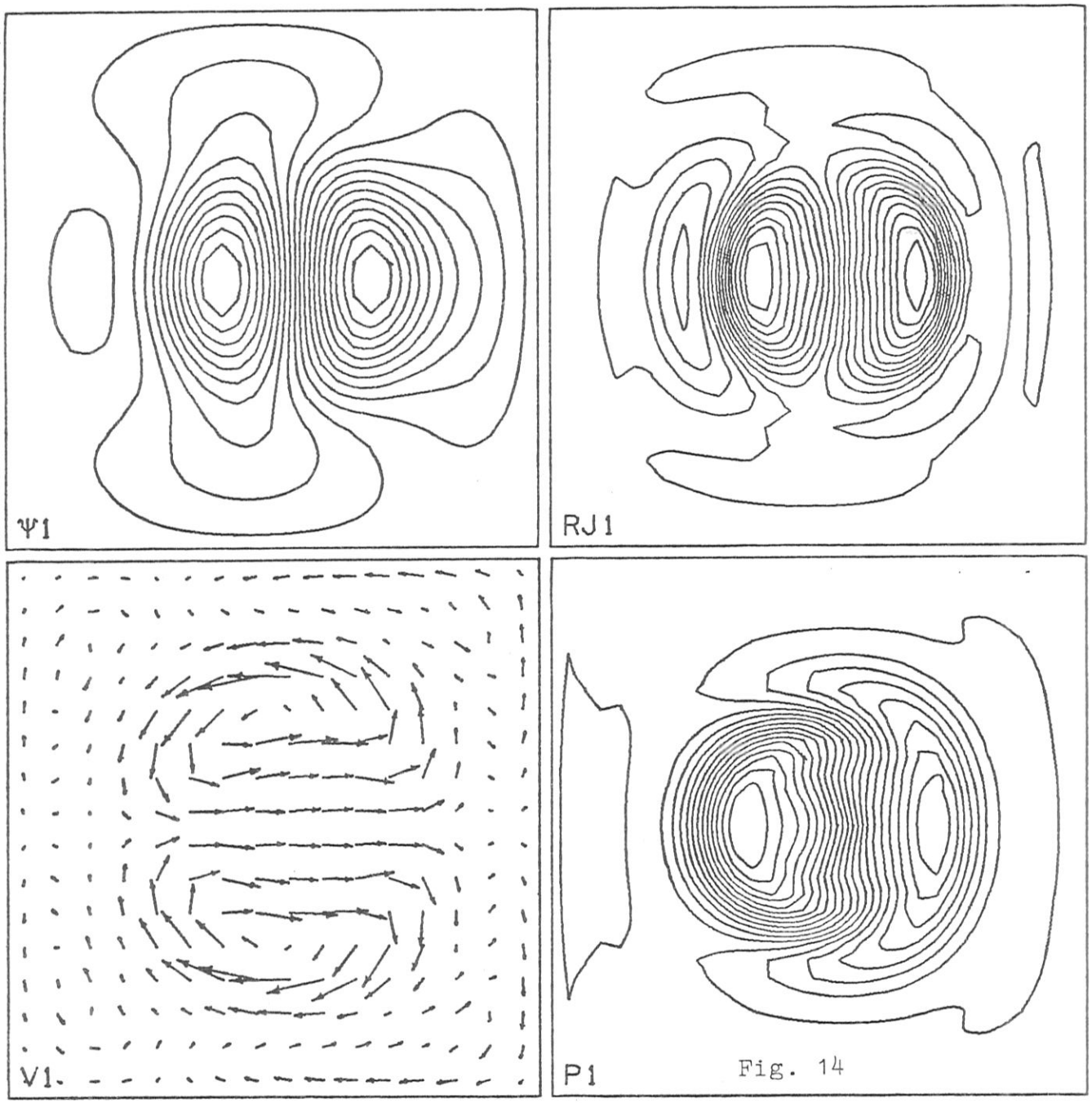

Fig. 14

N =	32	μ = 5
M =	31	
ε =	0.300	
Δ t =	0.020	
β =	0.050	
ν =	0.100E-03	
η_o =	0.100E-02	
Φ_o =	0.100E-02	
Ψ_o =	5.000	
$\Psi 1_o$ =	0.1000	
φ =	0.000	
T =	150.0000	
$\Psi 1_M$ =	0.525E-01	
$J1_M$ =	0.238E 01	
$U1_M$ =	0.107E-01	
$P1_M$ =	0.637E 00	
m =	1	

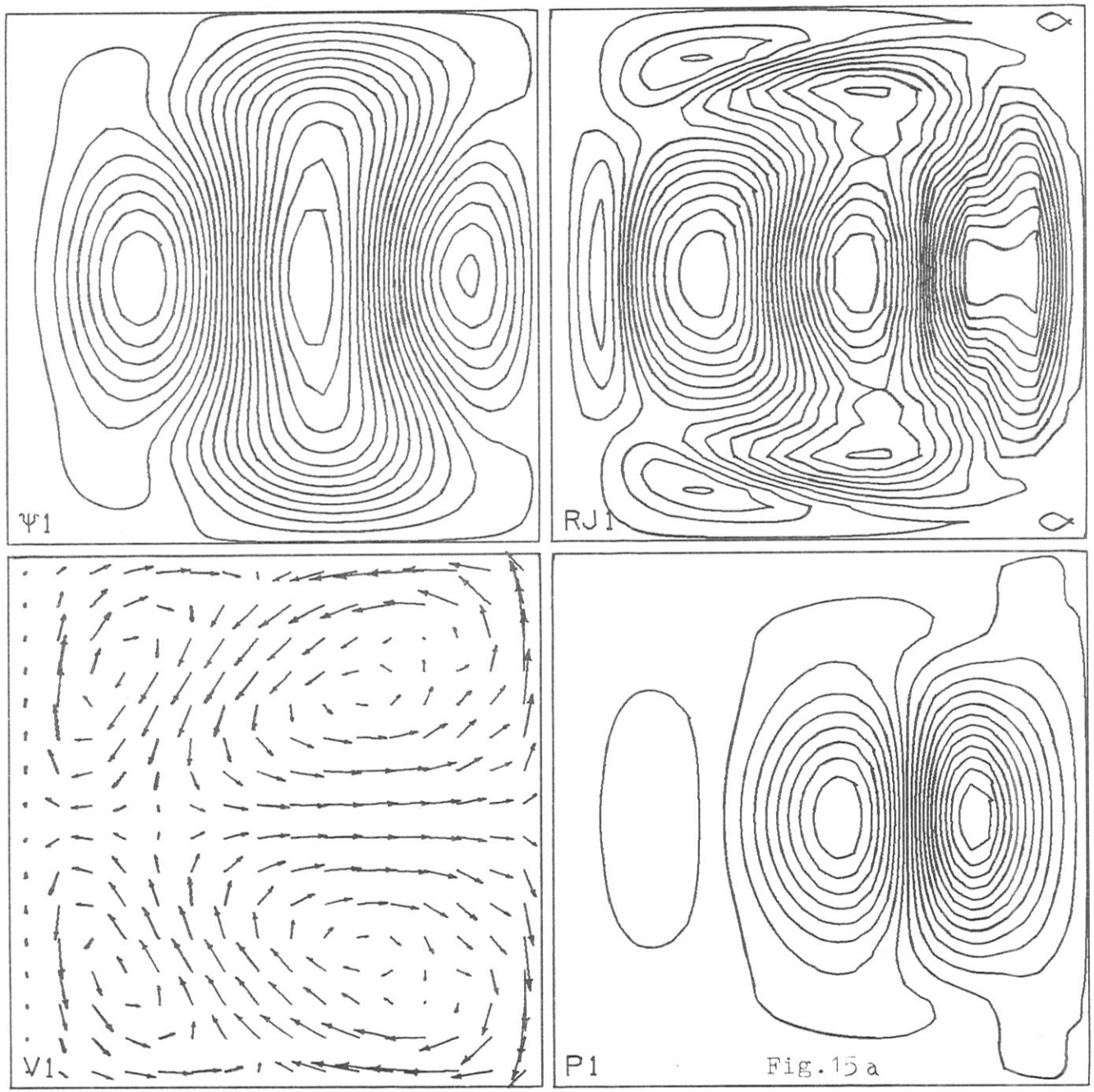

Fig. 15 a

$N = 32 \qquad \mu = 2$

$M = 32$

$\varepsilon = 0.000$

$\Delta t = 0.050$

$\beta = 1.000$

$\nu = 0.0$

$\eta_0 = 0.100E-02$

$\Phi_0 = 0.100E-02$

$J_0 = 5.000$

$\Psi 1_0 = 0.1000$

$\phi = 0.000$

$T = 100.0000$

$\Psi 1_M = 0.987E\ 01$

$J1_M = 0.238E\ 03$

$U1_M = 0.240E\ 01$

$P1_M = 0.367E\ 02$

$m = 1$

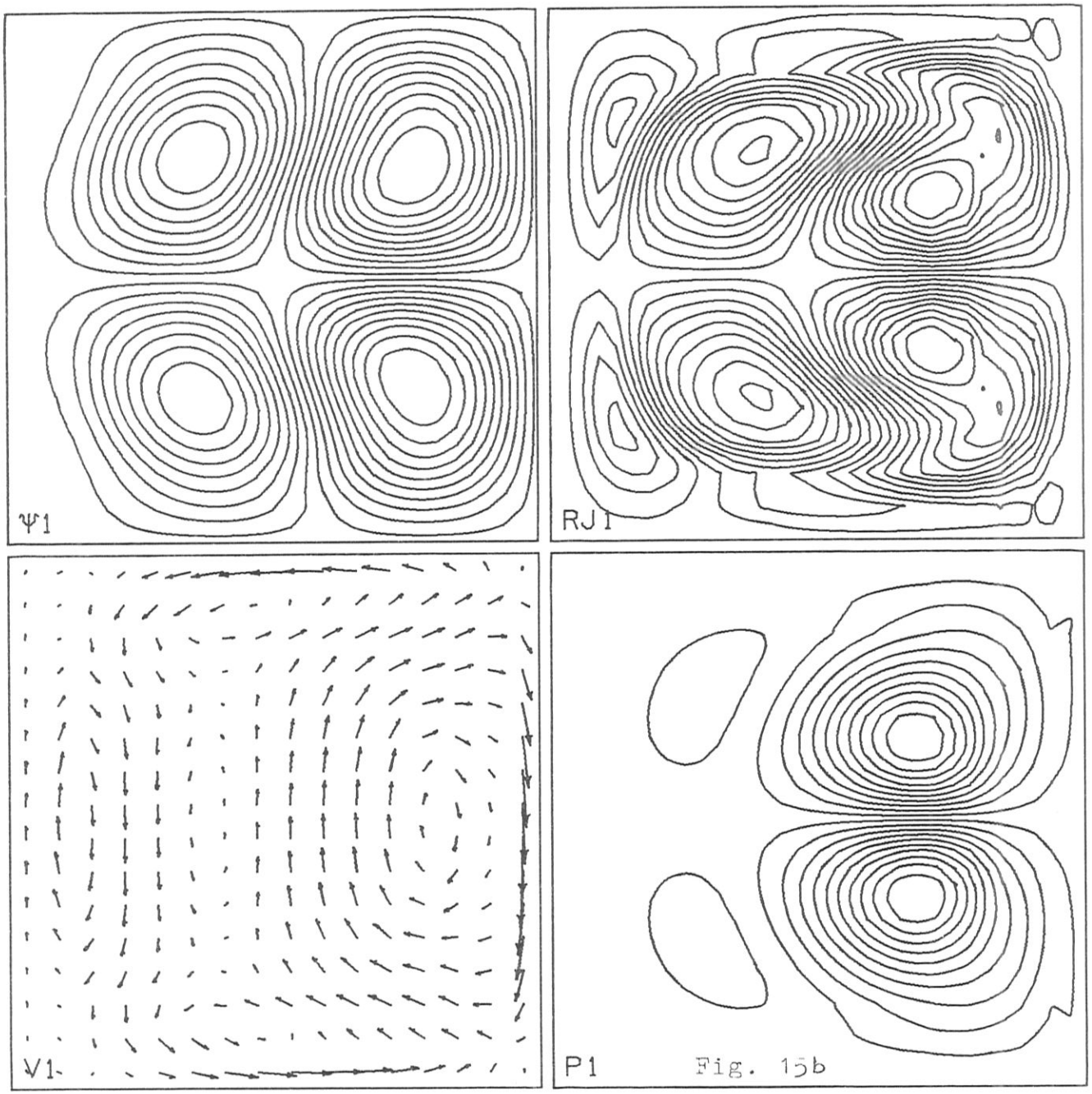

Fig. 15b

N =	32	μ = 2
M =	32	
ε =	0.000	
Δ t =	0.050	
β =	1.000	
ν =	0.0	
η_0 =	0.100E-02	
Φ_0 =	0.100E-02	
J_0 =	5.000	
$\Psi 1_0$ =	0.1000	
φ =	90.000	
T =	100.0000	
$\Psi 1_M$ =	0.816E 01	
$J1_M$ =	0.222E 03	
$U1_M$ =	0.321E 01	
$P1_M$ =	0.311E 02	
m =	1	

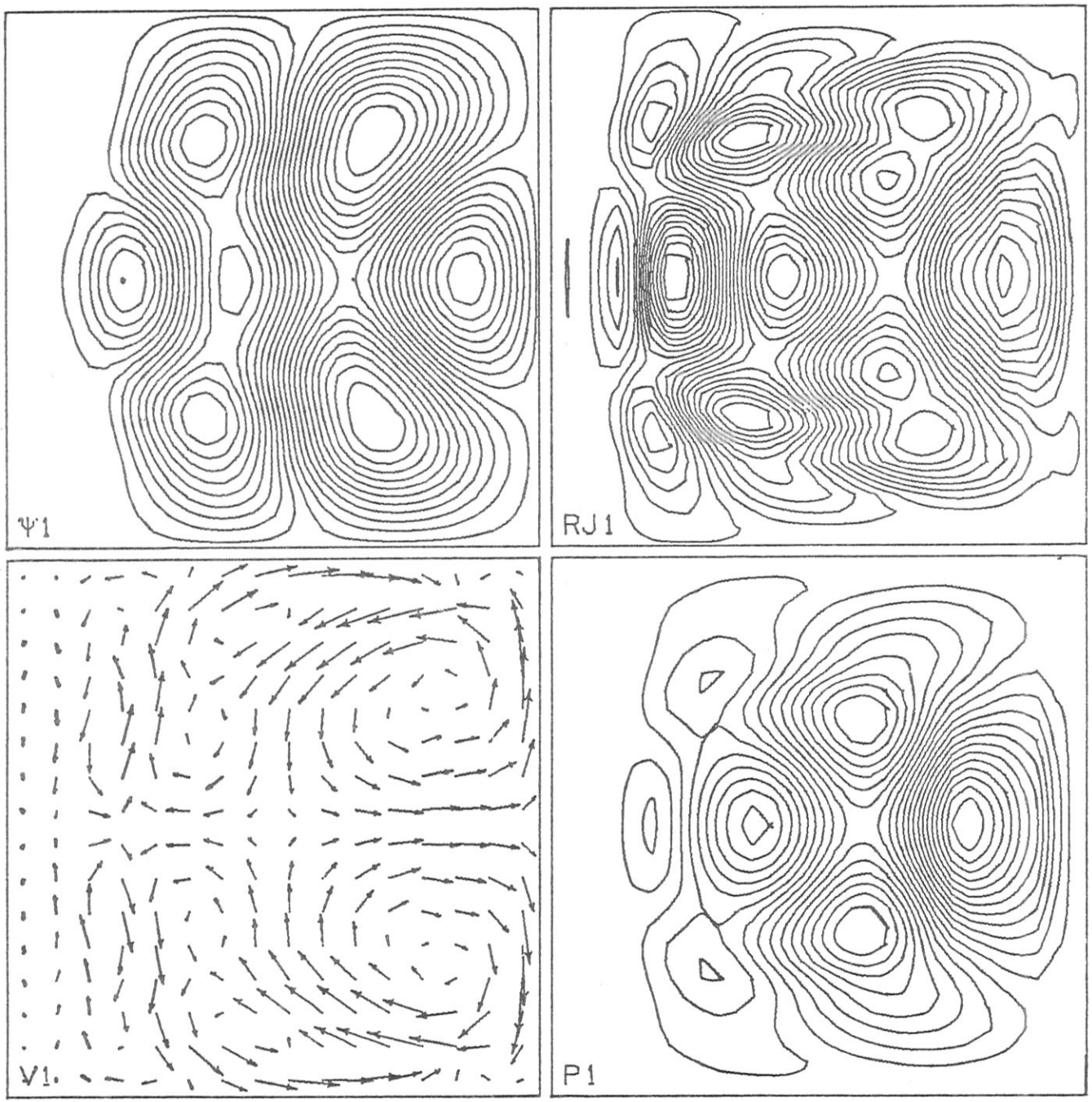

Fig. 16

N =	32	μ = 5
M =	31	
ε =	0.200	
Δ t =	0.020	
β =	0.500	
ν =	0.100E-03	
η_0 =	0.100E-02	
Φ_0 =	0.100E-02	
Ψ_0 =	2.500	
$\Psi 1_0$ =	0.1000	
φ =	0.000	
T =	200.0000	
$\Psi 1_M$ =	0.113E 01	
$J1_M$ =	0.530E 02	
$U1_M$ =	0.664E 00	
$P1_M$ =	0.474E 01	
m =	1	

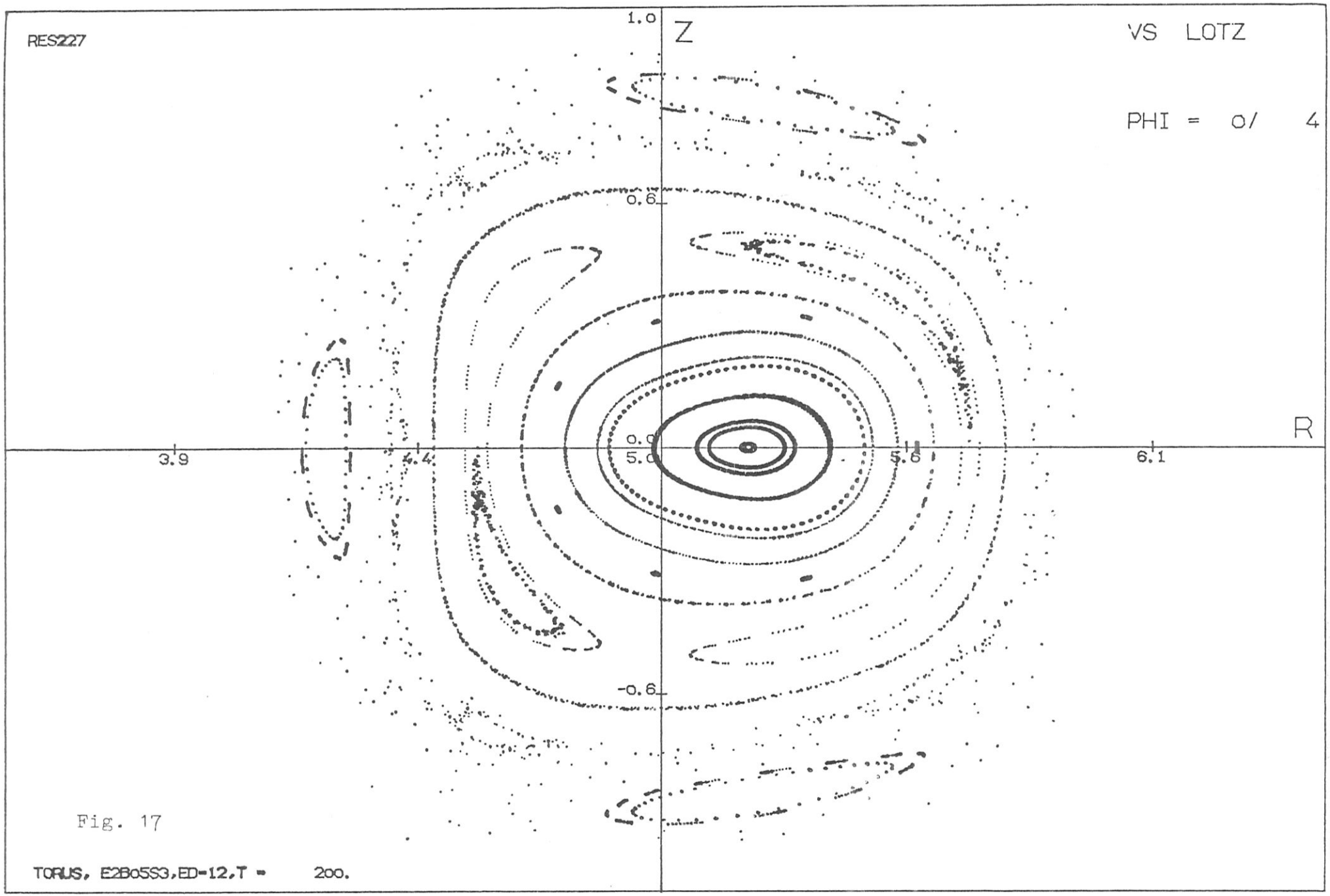
RES227
Z
VS LOTZ
PHI = 0/ 4
1.0
0.6
0.0
-0.6
3.9
4.4
5.0
5.6
6.1
R
TORUS, E2B05S3,ED-12,T = 200.

Fig. 17

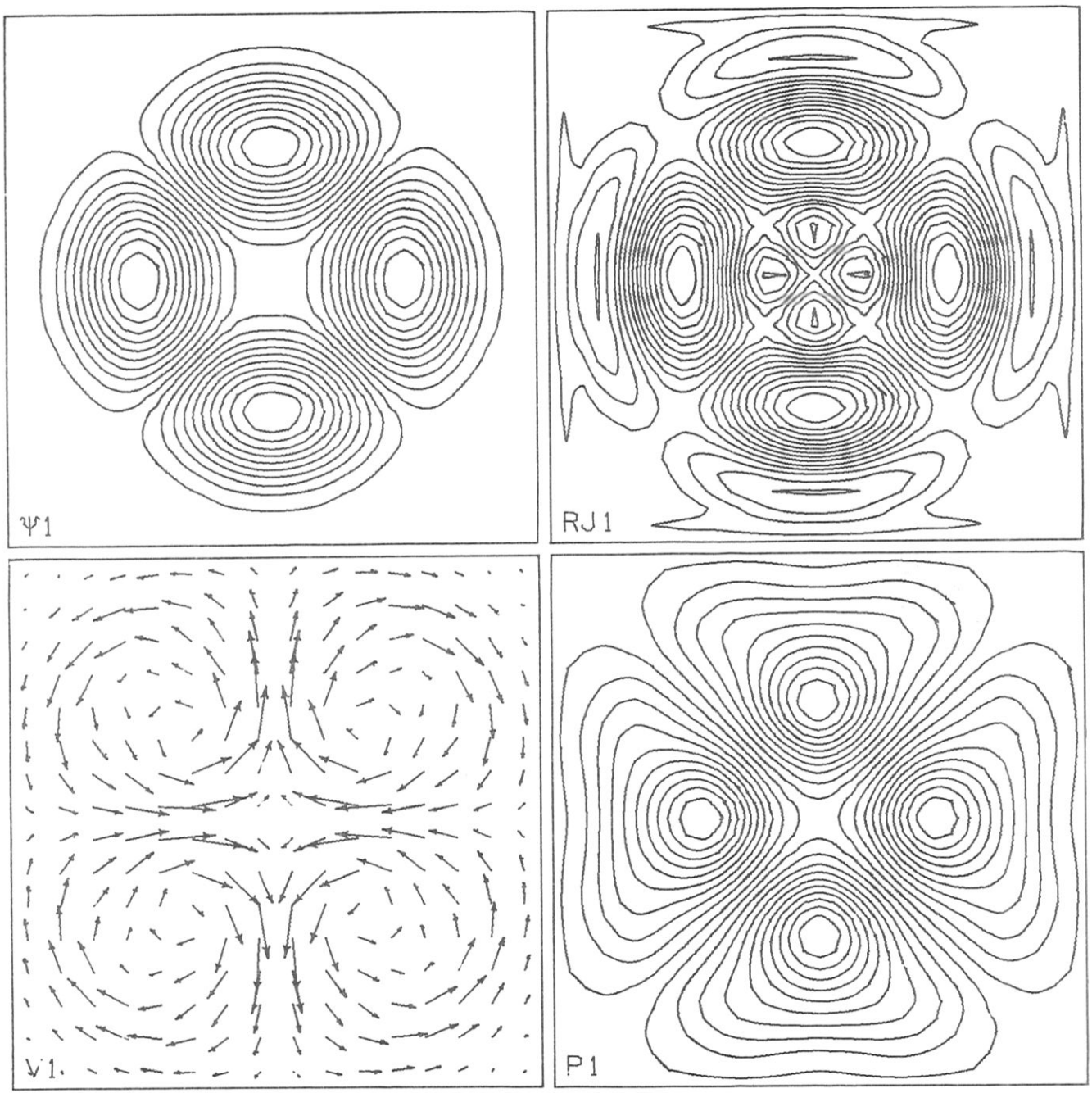

Fig. 18

N =	32	μ = 0
M =	32	
ε =	0.000	
Δ t =	0.100	
β =	0.000	
ν =	0.0	
η_0 =	0.0	
Φ_0 =	0.0	
J_0 =	1.300	
$\Psi 1_0$ =	0.1000	
φ =	0.000	
T =	1.0000	
$\Psi 1_M$ =	0.387E-03	
$J1_M$ =	0.192E-01	
$U1_M$ =	0.487E-04	
$P1_M$ =	0.222E-04	
m =	2	

Fig. 19 a

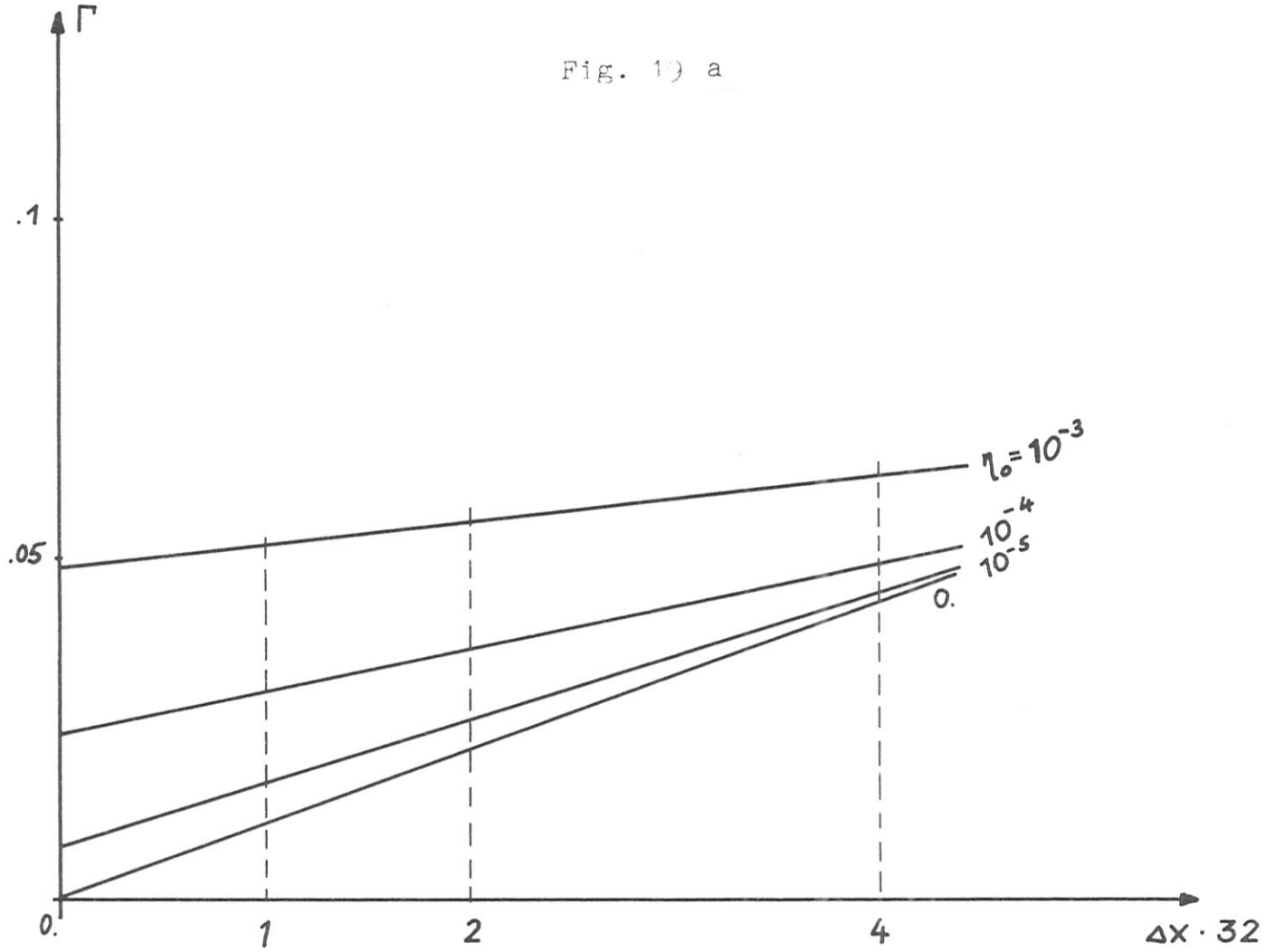

Fig. 19 b

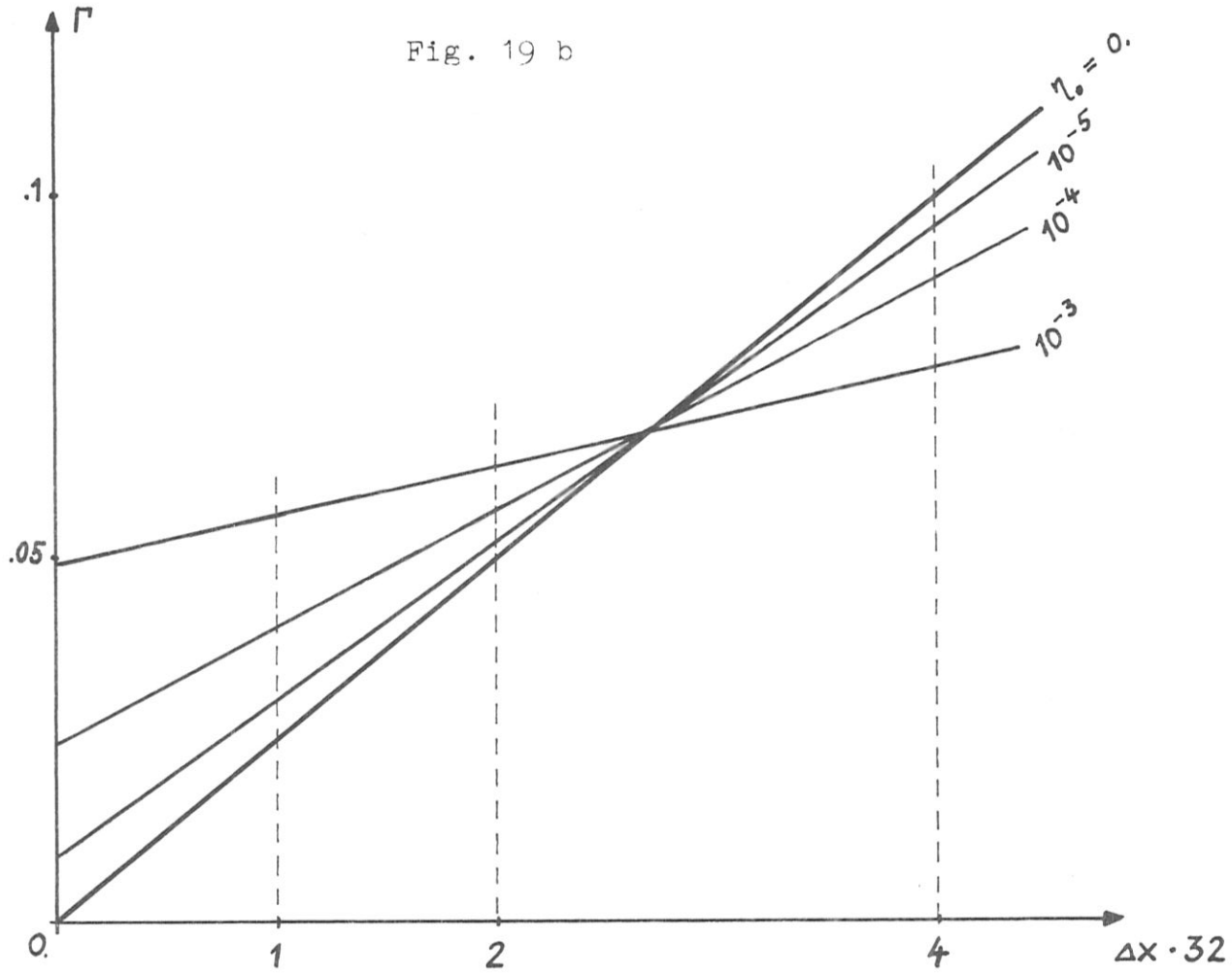

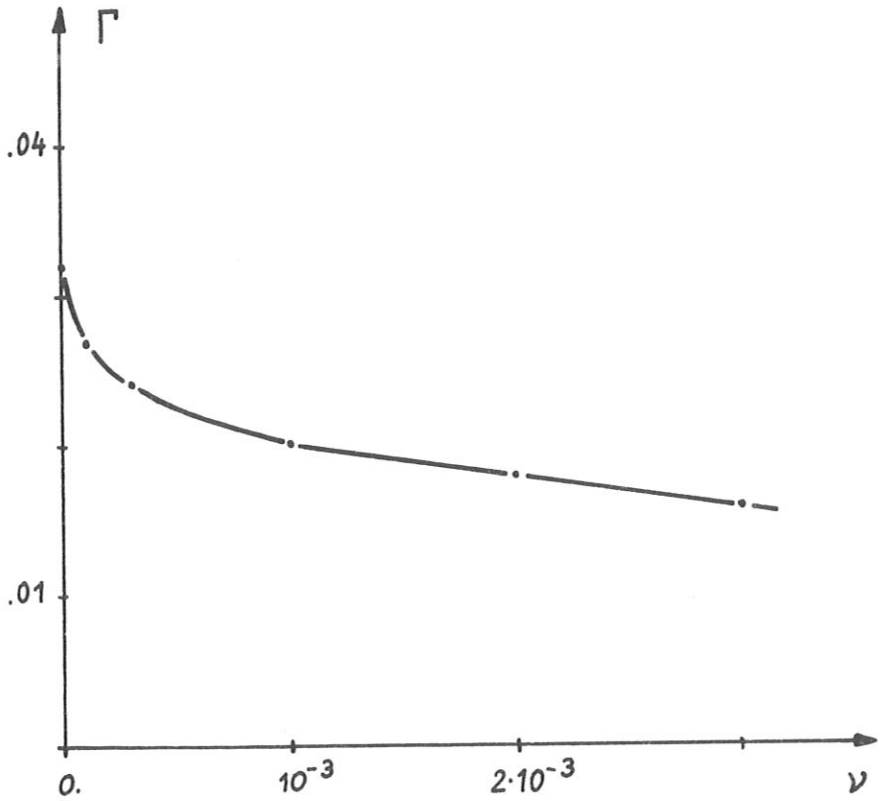

Fig. 2o

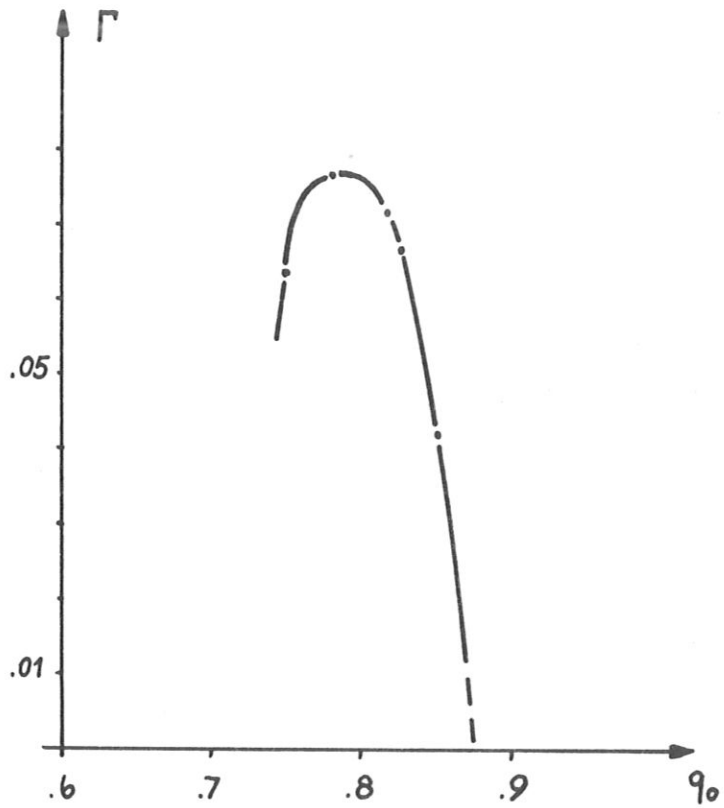

Fig. 21

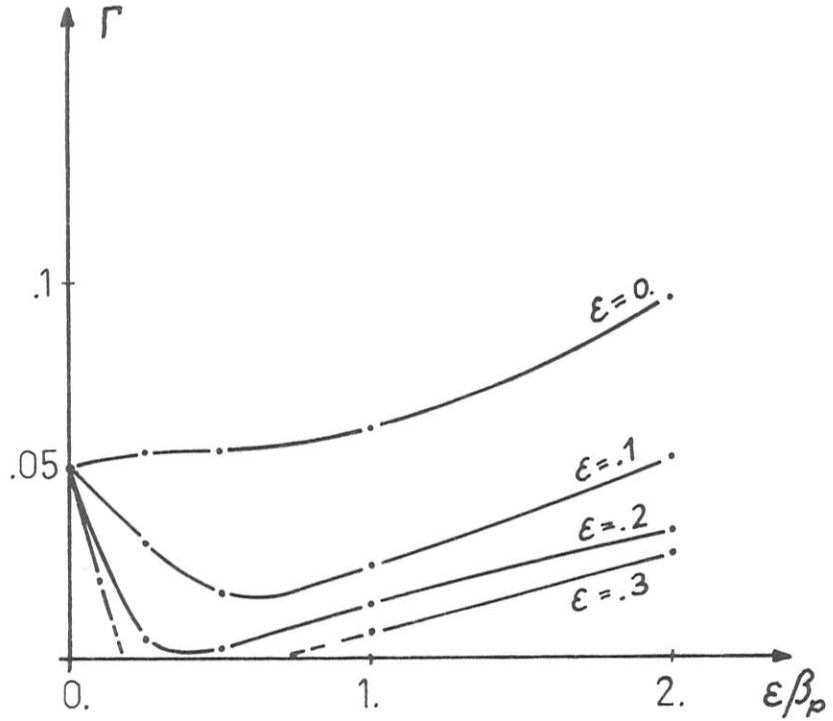

Fig. 22a

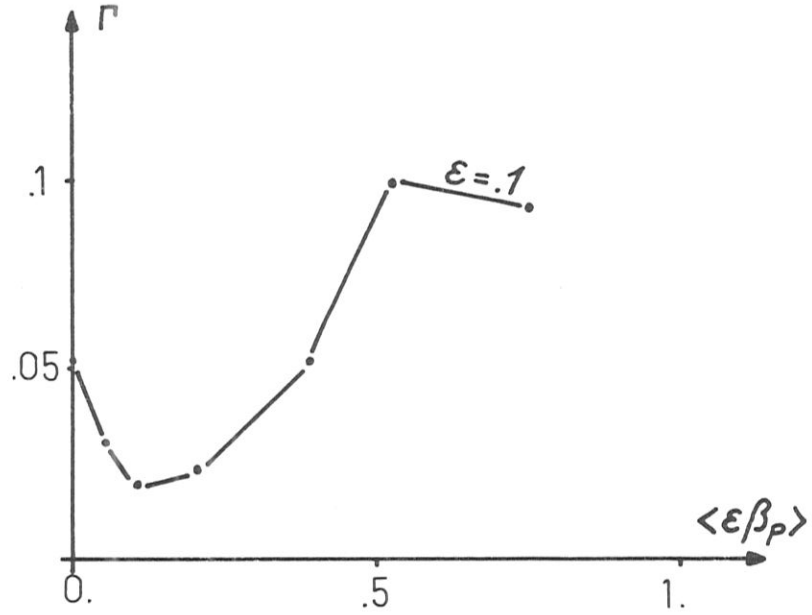

Fig. 22b

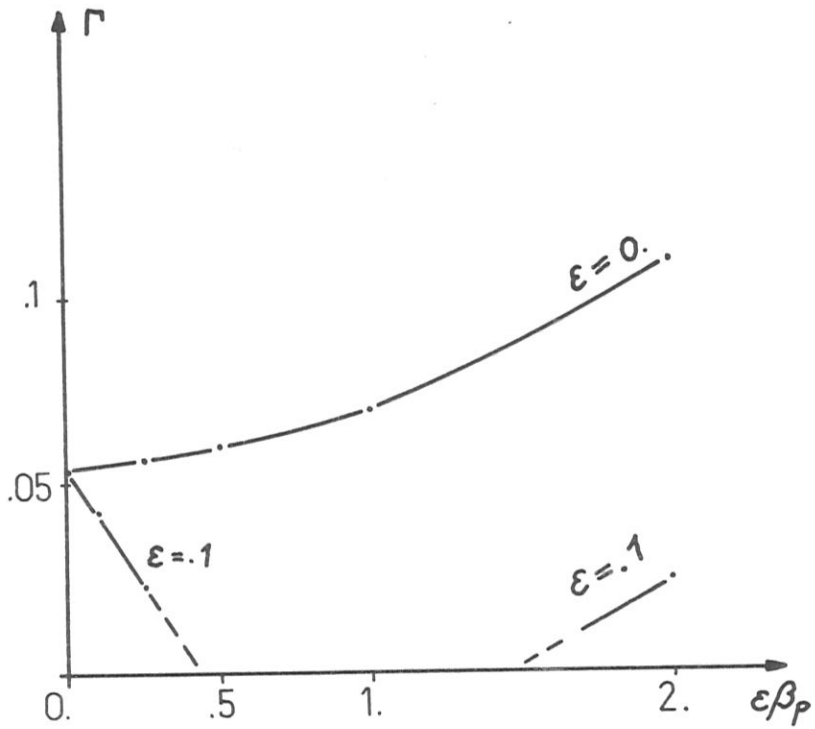

Fig. 23

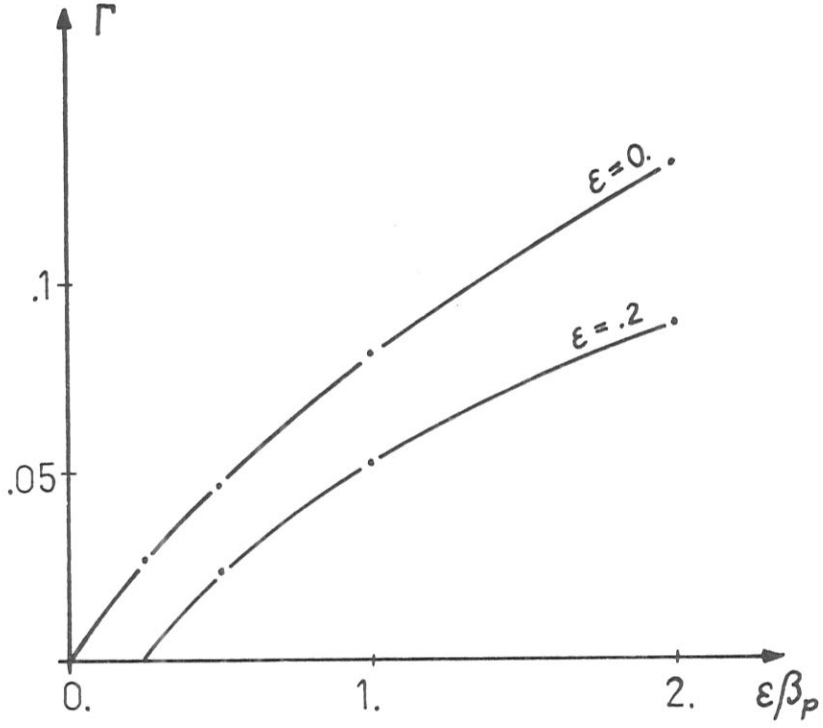

Fig. 24

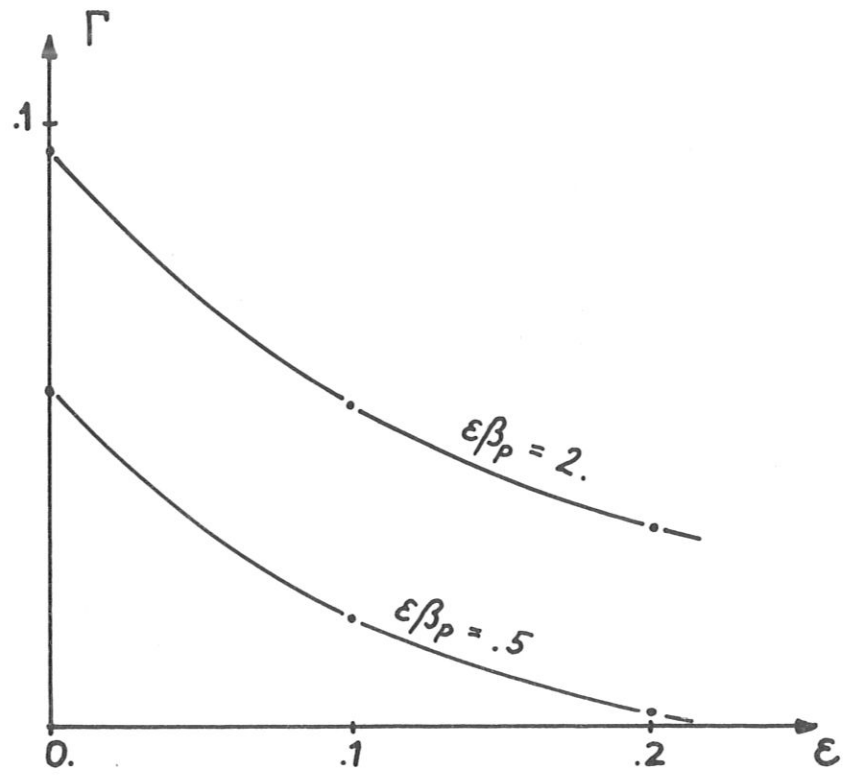

Fig. 25

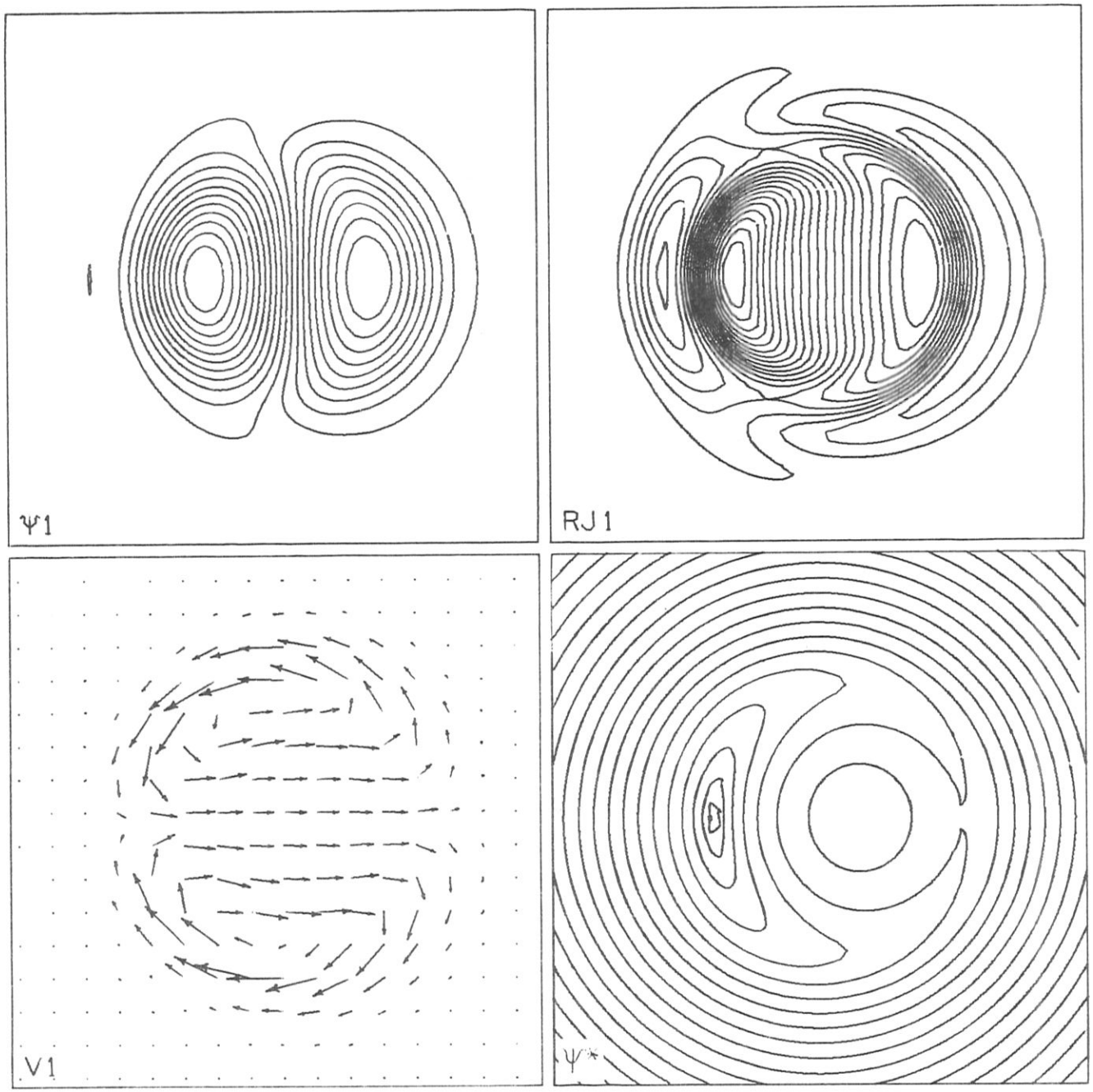

Fig 26a

$N = 64 \quad \mu = 2$

$M = 13$

$\varepsilon = 0.000$

$\Delta t = 0.010$

$\beta = 0.000$

$\nu = 0.0$

$\eta_0 = 0.100E-02$

$\Phi_0 = 0.100E-02$

$J_0 = 2.270$

$\Psi 1_0 = 0.1000$

$\phi = 0.000$

$T = 60.0000$

$\Psi 1_M = 0.470E-02$

$J1_M = 0.225E\ 00$

$U1_M = 0.306E-02$

$P1_M = 0.100E\ 01$

$m = 1$

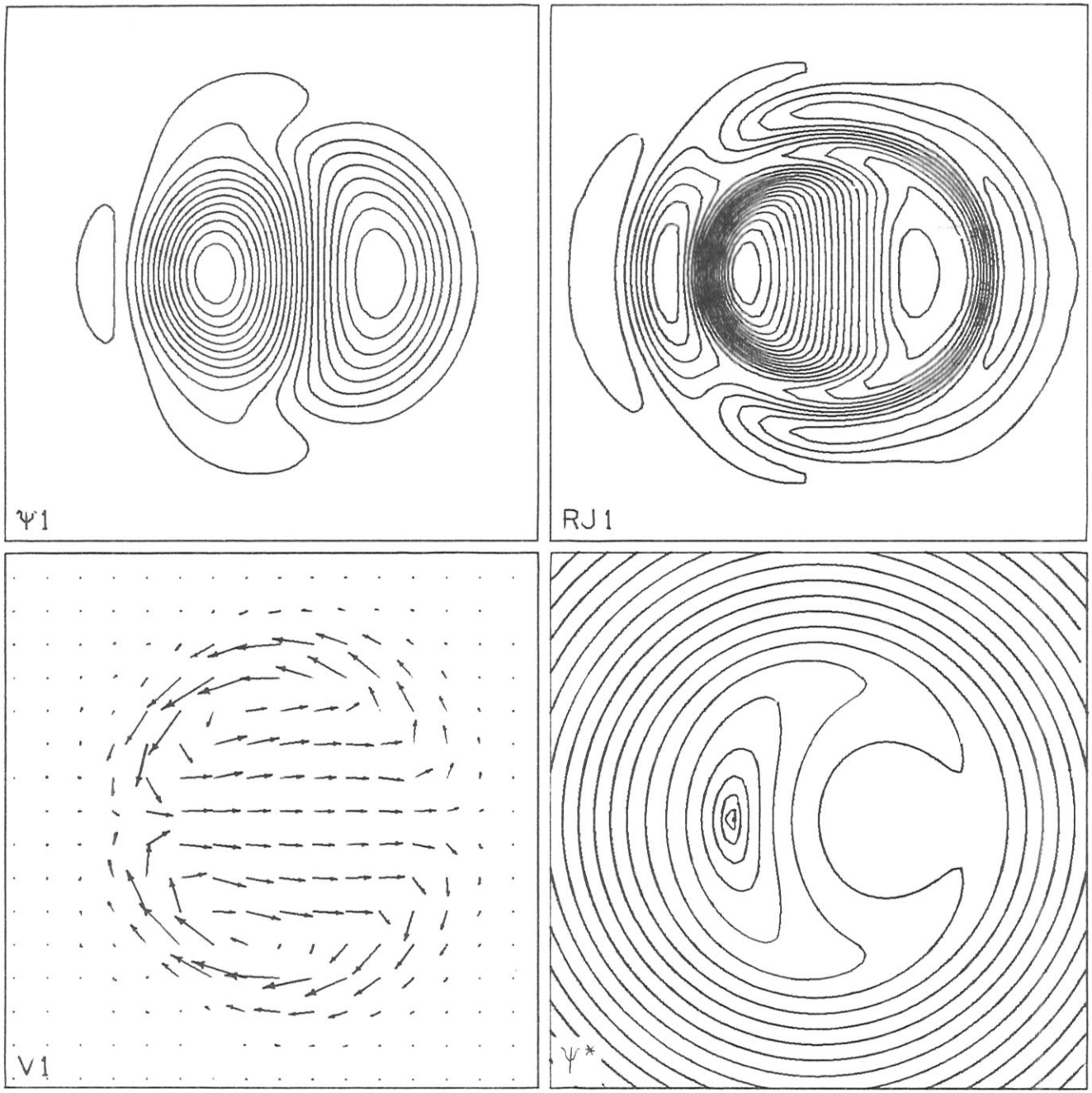

Fig. 26b

N = 64 μ = 2

M = 13

ε = 0.000

Δ t = 0.010

β = 0.000

ν = 0.0

η_0 = 0.100E-02

Φ_0 = 0.100E-02

J_0 = 2.270

$\Psi 1_0$ = 0.1000

φ = 0.000

T = 75.0000

$\Psi 1_M$ = 0.784E-02

$J1_M$ = 0.344E 00

$U1_M$ = 0.516E-02

$P1_M$ = 0.100E 01

m = 1

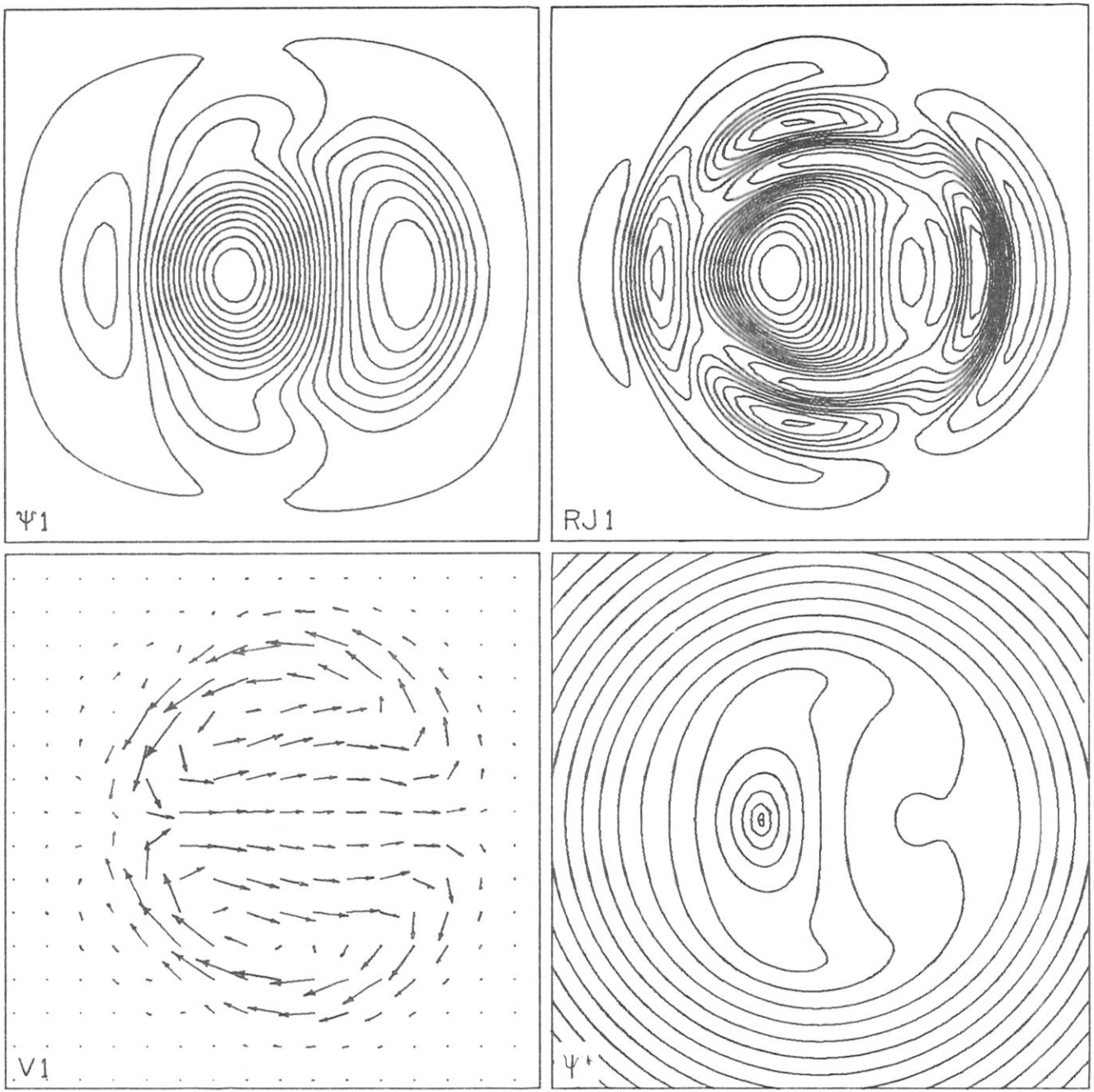

Fig. 26c

N = 64 μ = 2

M = 13

ε = 0.000

Δ t = 0.010

β = 0.000

ν = 0.0

η_0 = 0.100E-02

Φ_0 = 0.100E-02

J_0 = 2.270

$\Psi 1_0$ = 0.1000

φ = 0.000

T = 90.0000

$\Psi 1_M$ = 0.121E-01

$J1_M$ = 0.492E 00

$U1_M$ = 0.856E-02

$P1_M$ = 0.100E 01

m = 1

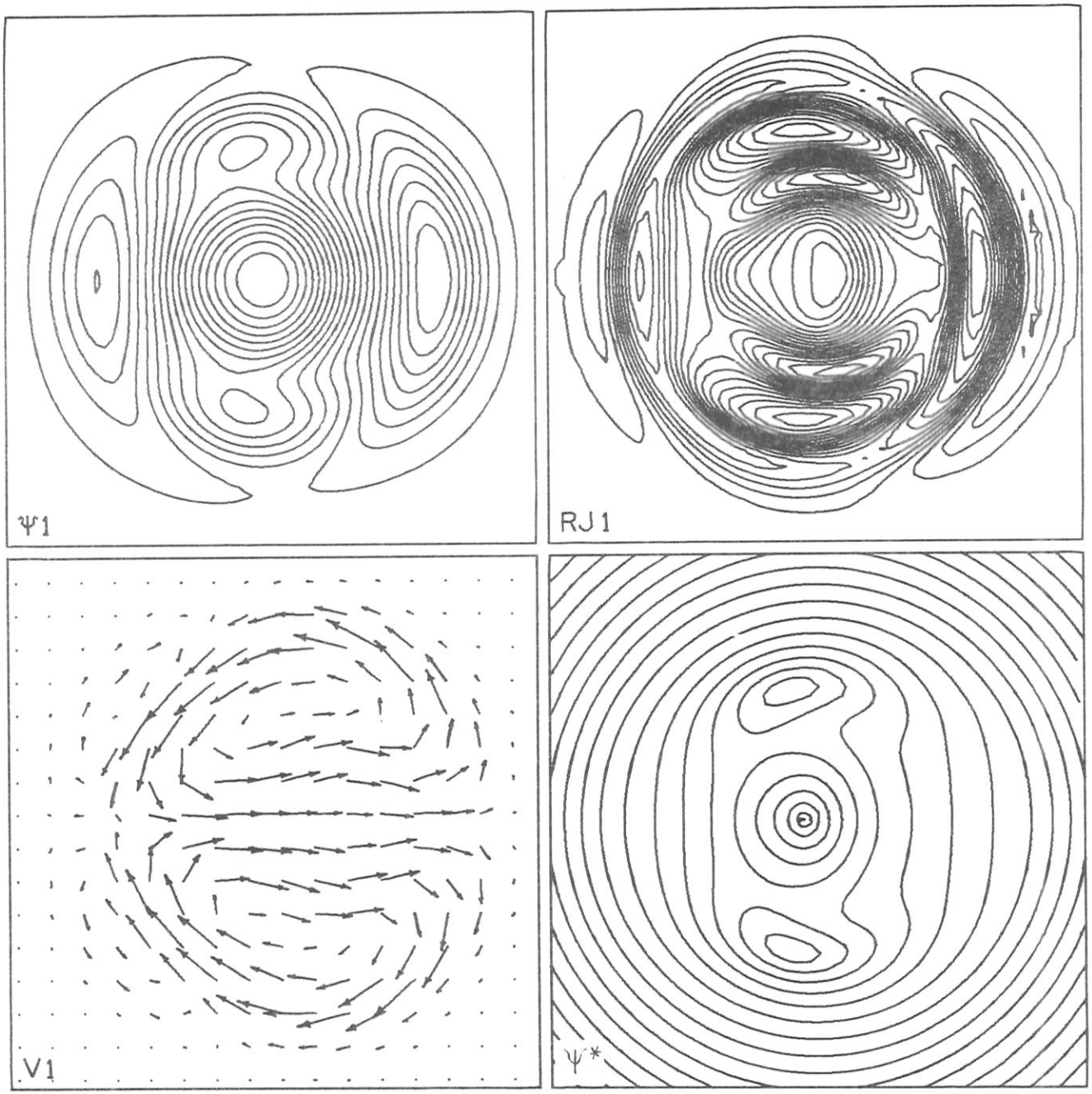

Fig. 26d

N = 64 μ = 2

M = 13

ε = 0.000

Δ t = 0.010

β = 0.000

ν = 0.0

η_0 = 0.100E-02

Φ_0 = 0.100E-02

J_0 = 2.270

$\Psi 1_0$ = 0.1000

φ = 0.000

T = 105.0000

$\Psi 1_M$ = 0.144E-01

$J1_M$ = 0.626E 00

$U1_M$ = 0.128E-01

$P1_M$ = 0.100E 01

m = 1

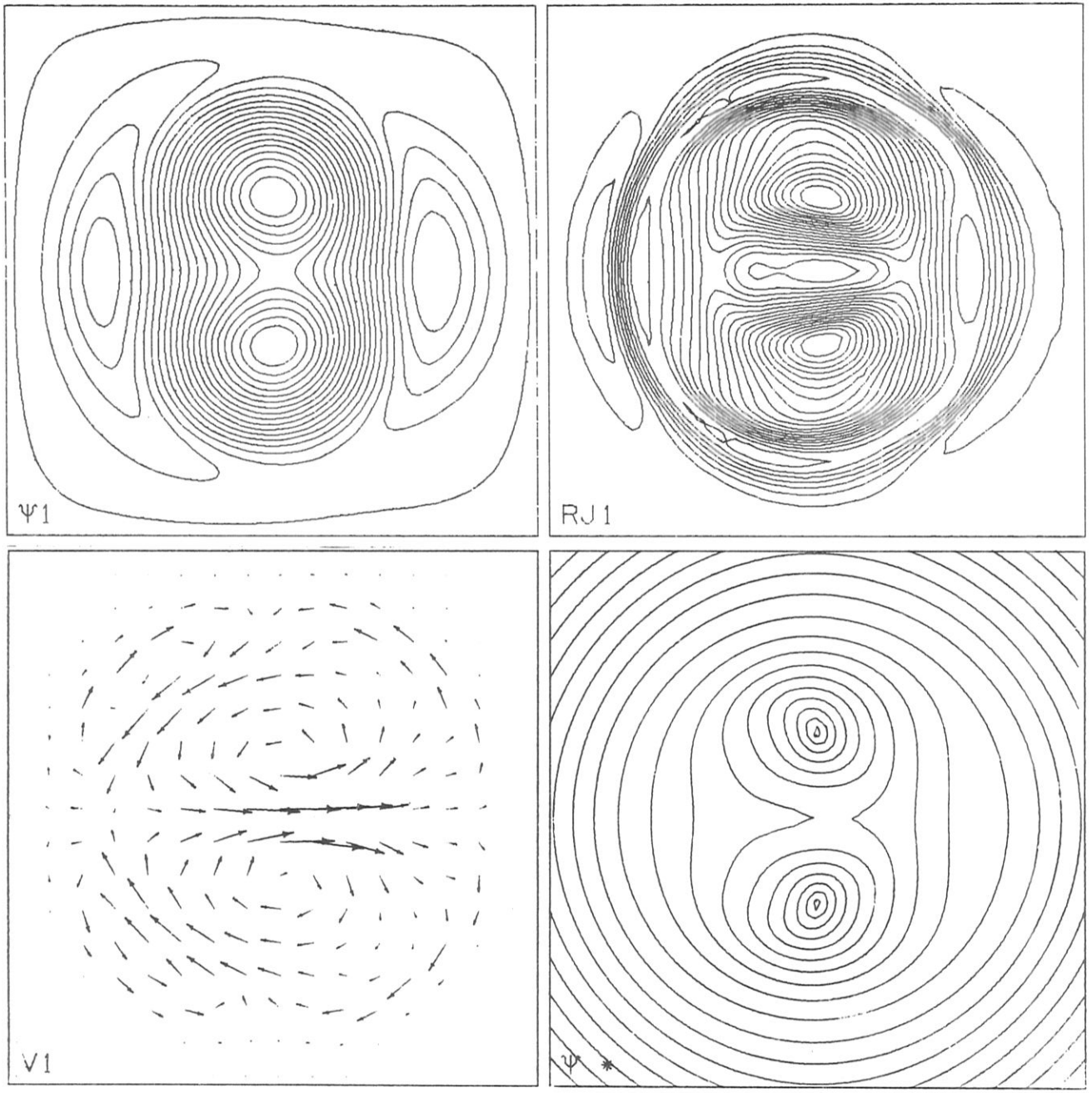

N = 64 μ = 2

M = 13

ε = 0.000

Δ t = 0.010

β = 0.000

ν = 0.0

η_0 = 0.100E-02

Φ_0 = 0.100E-02

J_0 = 2.270

$\Psi 1_0$ = 0.1000

φ = 0.000

T = 180.0000

$\Psi 1_M$ = 0.207E-01

$J 1_M$ = 0.816E 00

$U 1_M$ = 0.125E-01

$P 1_M$ = 0.100E 01

m = 1

Fig. 26e

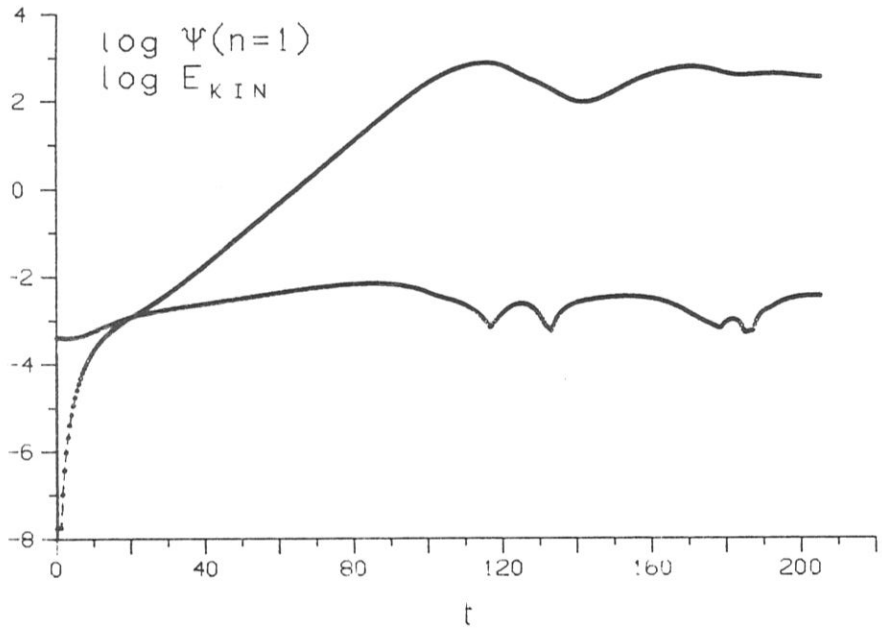
log Ψ(n=1)
log E KIN
4
2
0
-2
-4
-6
-8
0
40
80
120
160
200
t

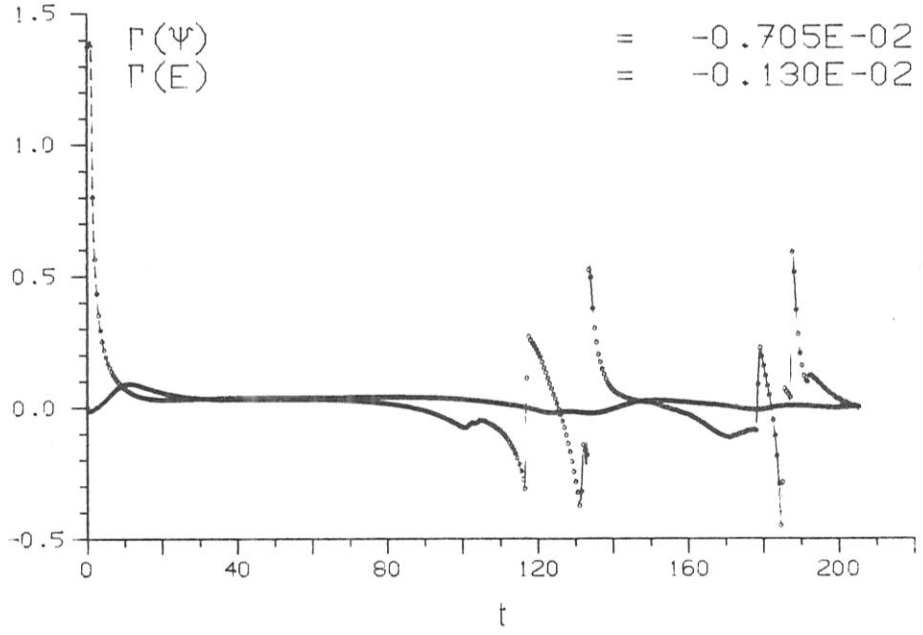
Γ(Ψ) = -0.705E-02
Γ(E) = -0.130E-02
1.5
1.0
0.5
0.0
-0.5
0
40
80
120
160
200
t

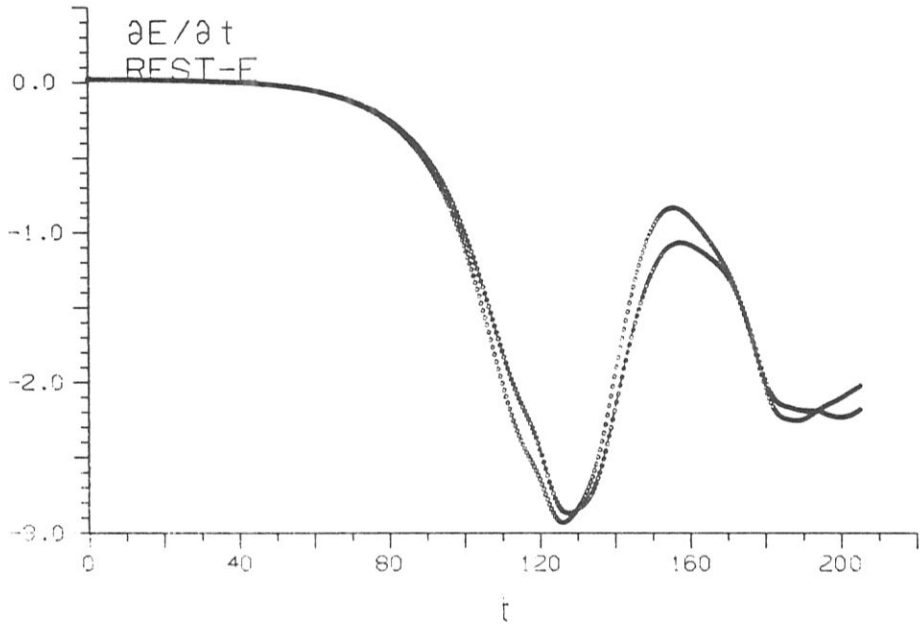
∂E/∂t
REST-F
0.0
-1.0
-2.0
-3.0
0
40
80
120
160
200
t

Fig 27

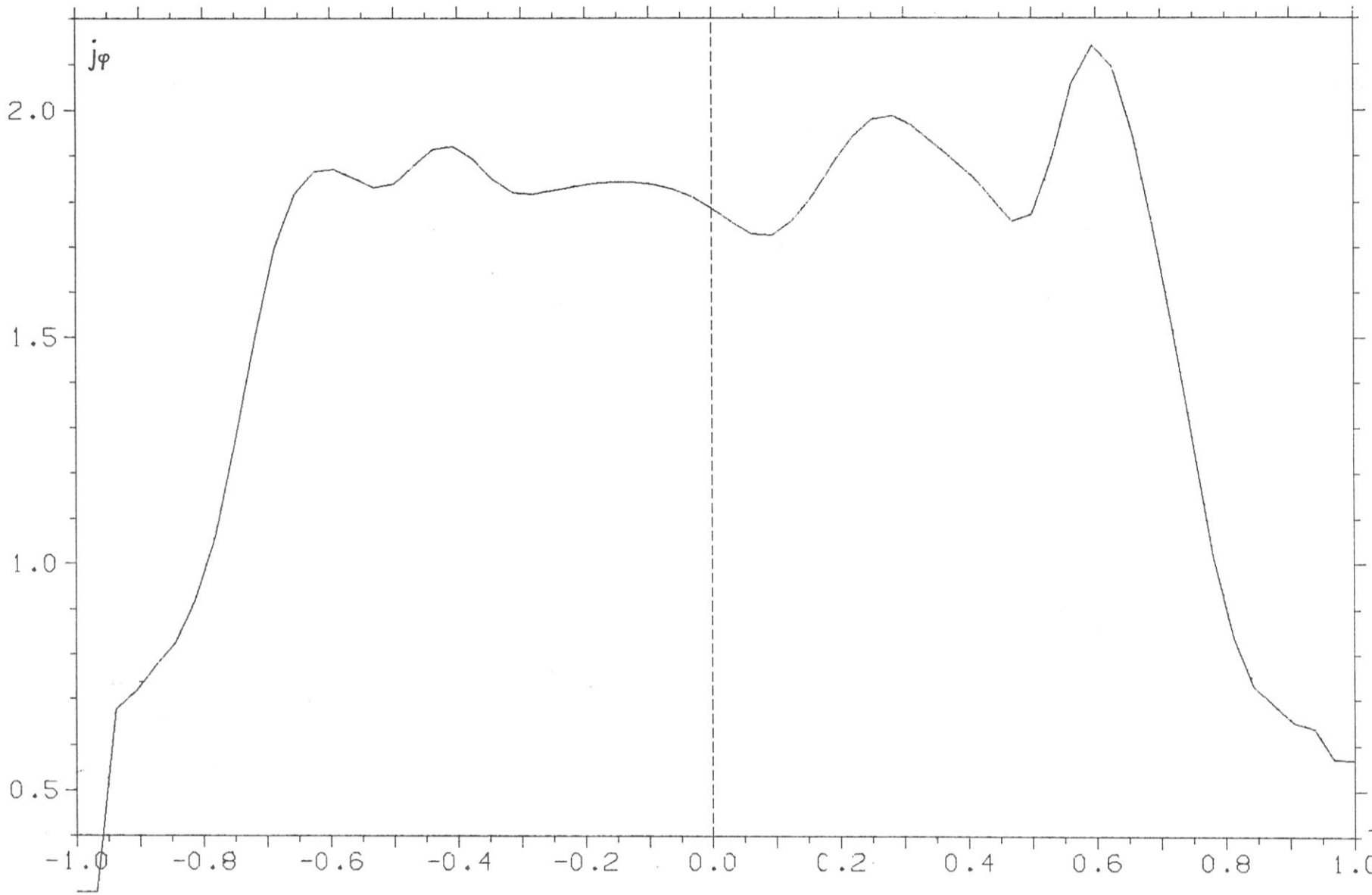

Fig. 28

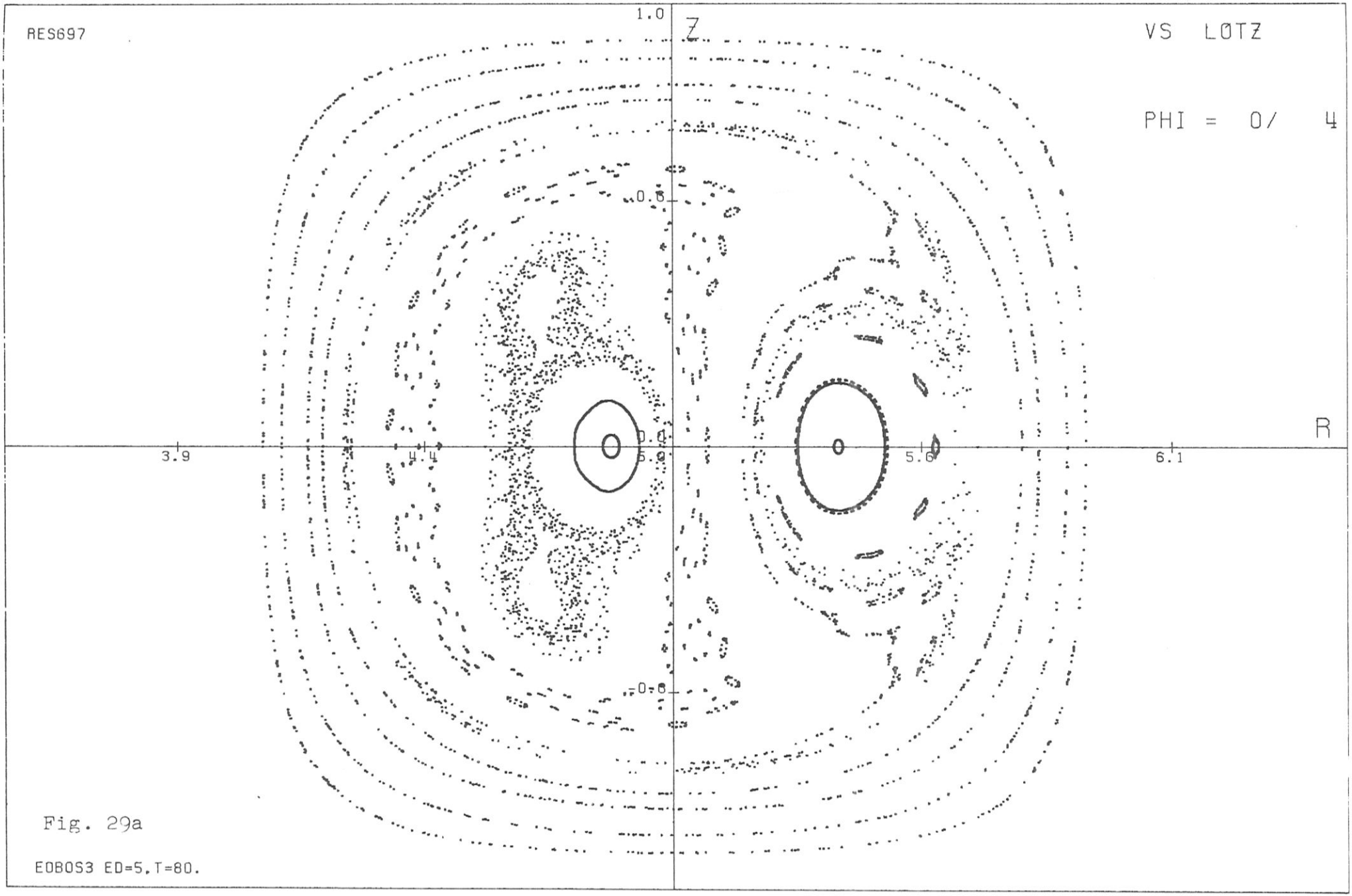

Fig. 29a

EOBOS3 ED=5,T=80.

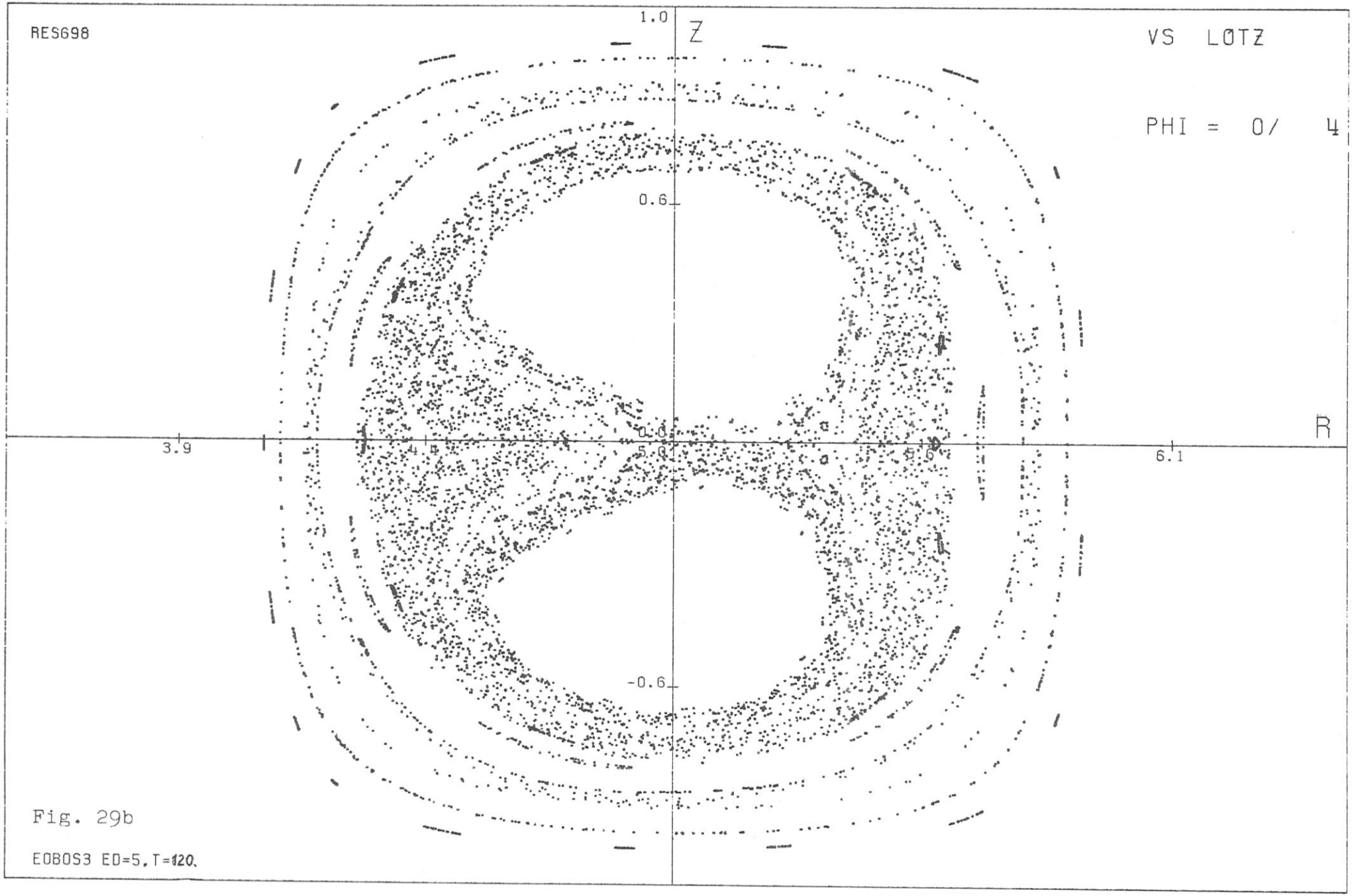

Fig. 29b

EOBOS3 ED=5. T=120.

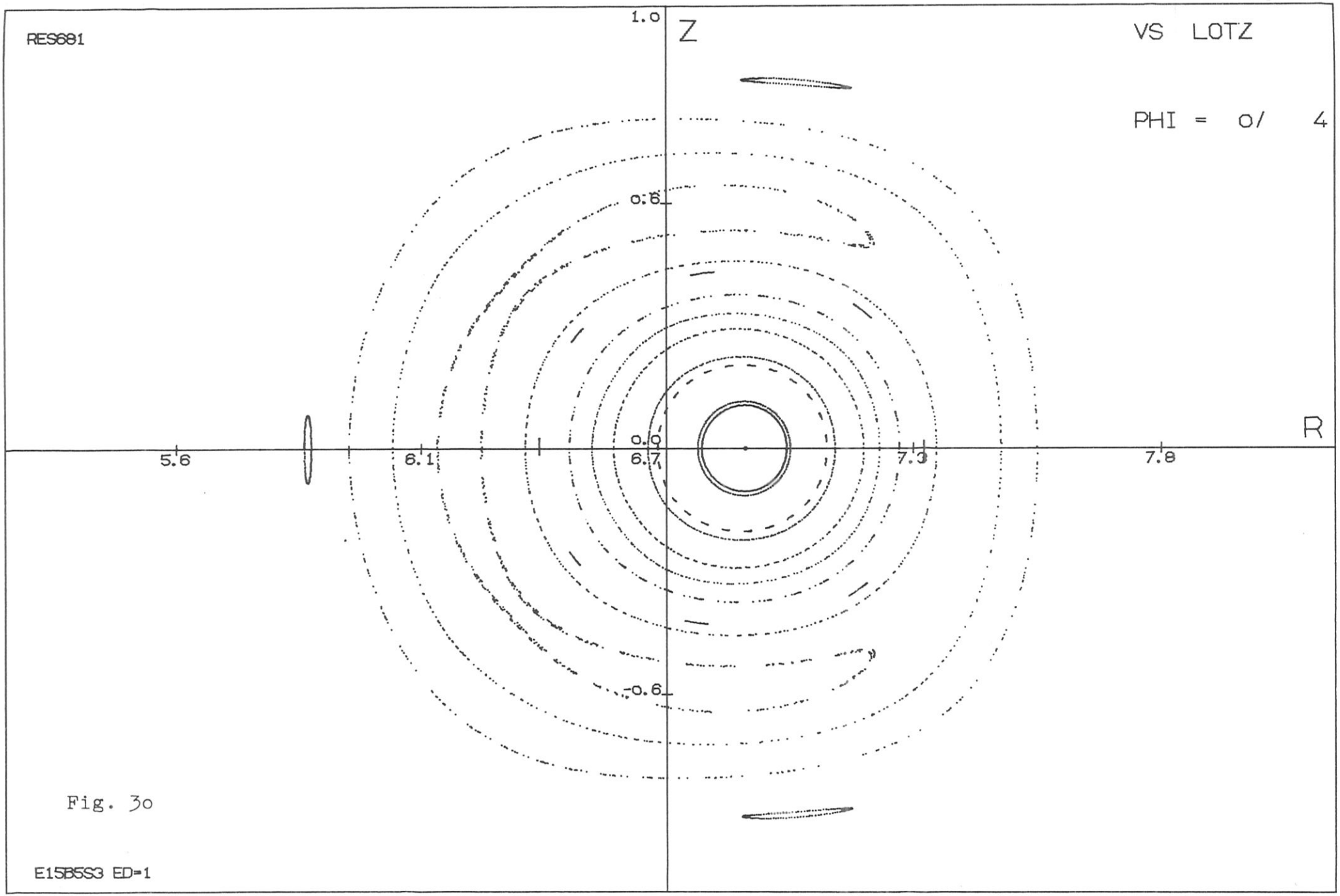

Fig. 3o

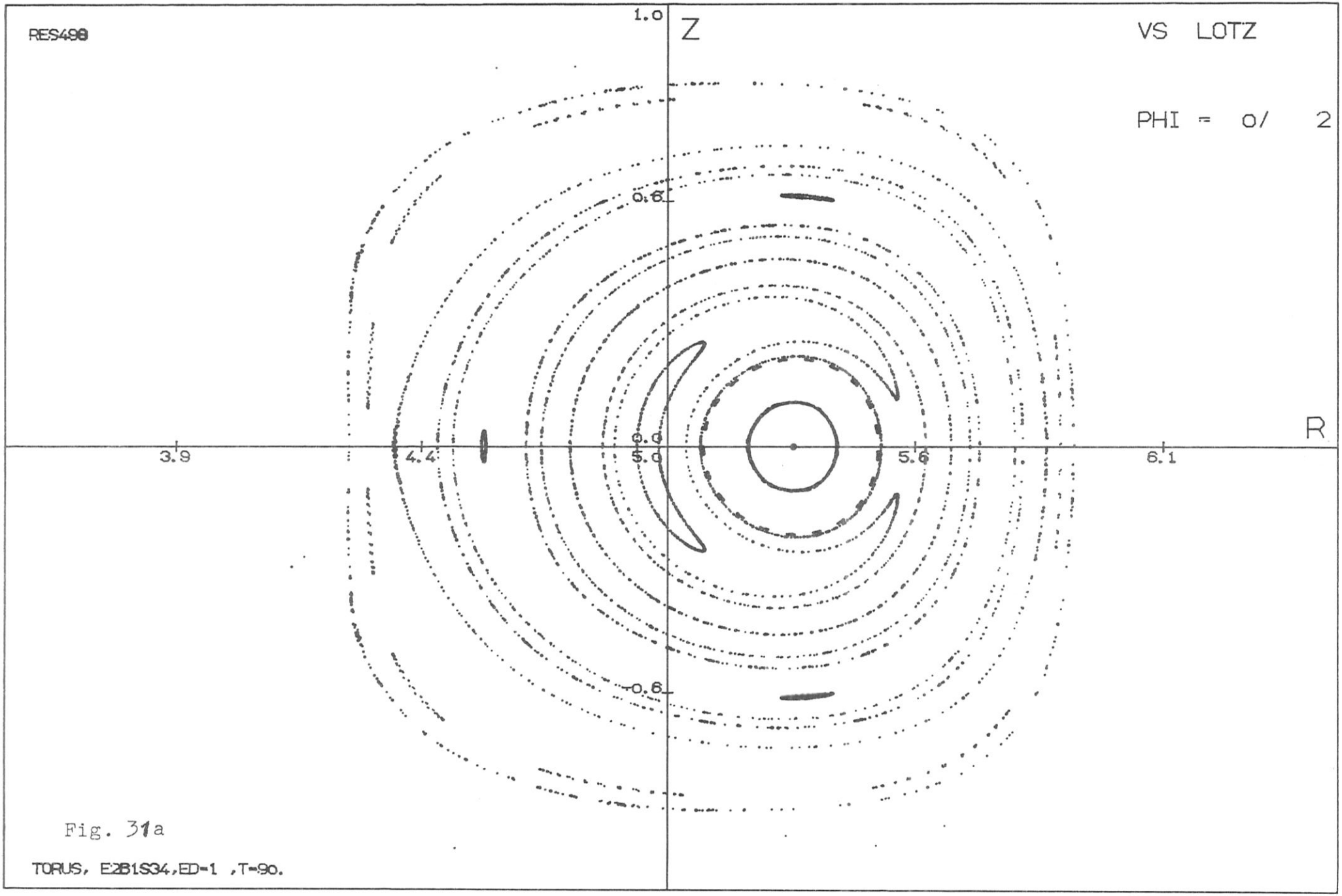

Fig. 31a

TORUS, E2B1S34,ED=1 ,T=90.

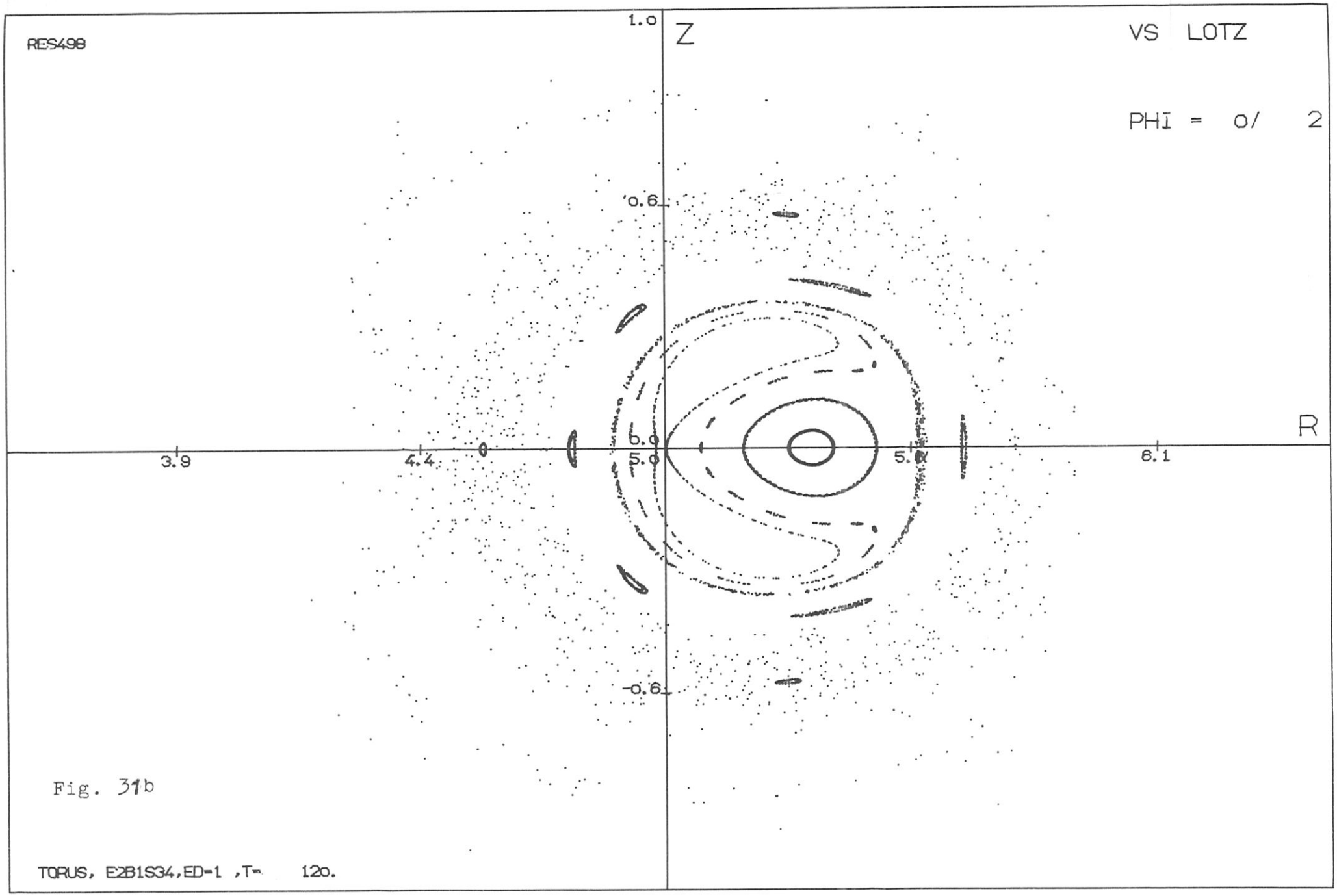
RES498
1.0
Z
VS LOTZ
PHI = 0/ 2
0.6
0.0
-0.6
3.9
4.4
5.0
5.
6.1
R
TORUS, E2B1S34,ED=1 ,T= 120.

Fig. 31b